Biological Sciences: Neuroscience

Pan-neuronal Imaging in Roaming *C. elegans*

Vivek Venkatachalam[1,2*], Ni Ji[1,2*], Xian Wang[1,2], Christopher M Clark[3], James Mitchell[1,2], Mason Klein[1,2], Christopher J Tabone[1,2], Jeremy T. Florman[3], Hongfei Ji[4], Joel SF Greenwood[2], Andrew D. Chisholm[5], Jagan Srinivasan[6], Mark J Alkema[3,†], Mei Zhen[7,†], Aravinthan DT Samuel[1,2,†]

[1] Department of Physics, Harvard University, Cambridge, Massachusetts, 02138 USA
[2] Center for Brain Science, Harvard University, Cambridge, Massachusetts, 02138 USA
[3] Department of Neurobiology, University of Massachusetts Medical School, Worcester, Massachusetts, 01605 USA
[4] Department of Physics, Nanjing University, Nanjing, China
[5] Division of Biological Sciences, Section of Neurobiology, University of California San Diego, La Jolla, CA 92093 USA
[6] Department of Biology and Biotechnology, Worcester Polytechnic Institute, Worcester, MA 01609
[7] Samuel Lunenfeld Research Institute, Mount Sinai Hospital, Toronto, ON, Canada M5G 1X5; and Departments of Molecular Genetics, and Physiology, University of Toronto, Toronto, ON, Canada M5S 1A8

[*]co-first authors
[†]co-senior authors

Correspondence to Vivek Venkatachalam: vivek@physics.harvard.edu

We present an imaging system for panneuronal recording in crawling *C. elegans*. A spinning disk confocal microscope, modified for automated tracking of the *C. elegans* head ganglia, simultaneously records the activity and position of ~80 neurons that co-express cytoplasmic calcium indicator GCaMP6s and nuclear localized RFP at 10 volumes per second. We developed a behavioral analysis algorithm that maps the movements of the head ganglia to the animal's posture and locomotion. Image registration and analysis software automatically assigns an index to each nucleus and calculates the corresponding calcium signal. Neurons with highly stereotyped positions can be associated with unique indexes and subsequently identified using an atlas of the worm nervous system. To test our system, we analyzed the brainwide activity patterns of moving worms subjected to thermosensory inputs. We demonstrate that our setup is able to uncover representations of sensory input and motor output of individual neurons from brainwide dynamics. Our imaging setup and analysis pipeline should facilitate mapping circuits for sensory to motor transformation in transparent behaving animals such as *C. elegans* and *Drosophila* larva.

Significance Statement:

A full understanding of sensorimotor transformation during complex behaviors requires quantifying brainwide dynamics of behaving animals. Here, we characterize brainwide dynamics of individual nematodes exposed to a defined thermosensory input. We show that it is possible to uncover representations of sensory input and motor output in individual neurons of behaving animals. Panneuronal imaging in roaming animals will facilitate systems neuroscience in behaving *C. elegans.*

\body

Introduction

Understanding how brain dynamics creates behaviors requires quantifying the flow and transformation of sensory information to motor output in behaving animals. Optical imaging using genetically encoded calcium or voltage fluorescent probes offers a minimally invasive method to record neural activity in intact animals. The nematode *C. elegans* is particularly ideal for optical neurophysiology owing to its small size, optical transparency, compact nervous system, and ease of genetic manipulation. Imaging systems for tracking the activity of small numbers of neurons have been effective in determining their role during nematode locomotion and navigational behaviors like chemotaxis, thermotaxis, and the escape response (1-6). Recordings from large numbers of interconnected neurons are required to understand how neuronal ensembles carry out the systematic transformations of sensory input into motor patterns that build behavioral decisions.

Several methods for fast three-dimensional imaging of neural activity in a fixed imaging volume have been developed for different model organisms (7-14). High-speed light sheet microscopy, light field microscopy, multifocus microscopy, and two-photon structured illumination microscopy have proved effective for rapidly recording large numbers of neurons in immobilized, intact, transparent animals like larval zebrafish and nematodes (15-19). However, these methods are problematic when attempting to track many neurons within the bending and moving body of a behaving animal. Panneuronal recording in moving animals poses higher demands on spatial and temporal resolution. Furthermore, extracting neuronal signals from recordings in a behaving animal requires an effective analysis pipeline to segment image volumes into the activity patterns of discrete and identifiable neurons.

Here, we use high-speed spinning disk confocal microscopy – modified for automated tracking using real time image analysis and motion control software – to volumetrically image the head ganglia of behaving *C. elegans* adults at single-cell resolution. Our setup can simultaneously track ~80 neurons with 0.45 µm x 0.45 µm x 2 µm resolution at 10 Hz. Activity was reported by the ultrasensitive calcium indicator GCaMP6s expressed throughout the cytosol under the control of the panneuronal *rgef-1* promoter (a gift from D. Pilgrim) (20). To facilitate segmentation into individual identifiable neurons, nuclei were tracked using calcium insensitive, nuclear bound red fluorescent protein, TagRFP under the control of another panneuronal *rab-3* promoter (a gift from O. Hobert)(21). We developed an image analysis pipeline that converts the gross movements of the head into the time-varying position and posture of the crawling worm, and converts fluorescence measurements into near simultaneous activity patterns of all imaged neurons.

A similar approach to brainwide imaging in moving *C. elegans* using the same transgenic strain has recently been reported (22). While both setups use customized spinning disk confocal microscopes, the

strategies for tracking the moving neurons and analyzing behavioral and neural activity patterns are different. Nguyen et al. (2015) use a low power objective to track the posture of the animal and a high power objective to locate and image the nerve ring. The advantage of our single objective setup is that it affords the flexibility, for example, to deliver thermosensory inputs using an opaque temperature controlled stage below the animal. The advantage of low magnification imaging is that it provides a direct measurement of animal posture, which we must infer. These new technologies for pan-neuronal imaging in roaming animals now enables correlating brainwide dynamics to sensory inputs and motor outputs in transparent behaving animals like *C. elegans* and *Drosophila* larvae.

Results

Automated volumetric tracking of head ganglia in a moving worm

We built our imaging system into a spinning-disk confocal microscope (**Fig. 1a**). A custom-designed thermoelectric cooler was used to sinusoidally modulate the temperature of the stage over the course of an experiment to provide a defined thermosensory stimulus (**Fig. 1b**) (23). Individual young adult *C. elegans* were placed on a thin sheet of agar, covered with a large coverslip, and allowed to crawl between the agar and coverslip. A fast scientific CMOS camera (200 frames per second) and piezoelectric objective scanner (bi-directional rastering at 2 µm per step with 20 steps) provided an imaging rate of 10 volumes per second. We captured the image of each *z*-section in both red and green fluorescence emission channels using a dichroic to simultaneously project each channel onto different regions of the camera's sensor. When imaging with a 40x*,* 0.95 NA air objective, each volume represents 115 µm x 115 µm x 40 µm with pixel limited resolution of 0.45 µm x 0.45 µm x 2 µm. These imaging volumes and speeds were made possible using custom software written in MATLAB to control the microscope hardware, carrying out all functions including image capture, motion control, stimulus control, and data streaming.

A motorized stage kept a targeted image volume in the field of view at all times. This was achieved by real-time analysis of image volumes that sought and recognized the head ganglia in the green (GCaMP6s) channel. Fluctuations in the coordinates of the target in *x*, *y,* and *z* were used as difference signals to adjust the voltages applied to the stage and objective drivers to automatically keep the target in the center of the acquired volume. Feedback in *xy* ran at 10 Hz (every volume), and feedback in *z* ran at 2 Hz (every 5 volumes). The system was able to continuously image head ganglia of a crawling animal for up to 5 minutes without missing frames. The tracking system is described in detail in **Methods**.

Reconstructing a worm's motor behavior from head movement

To identify neural correlates of locomotory behavior, it is important to know both the posture and position of the body over time. Our setup tracks the position and orientation of the head ganglia of a crawling worm at high magnification. Some setups for tracking neural activity at high resolution implement a

second low magnification objective for simultaneous imaging of the worm body (24, 25). The advantage of single objective experimental designs is a simpler optical path that allows imaging the worm on an opaque substrate like our thermally controlled platform. A possible concern of single-objective imaging at high magnification is that our body measurement is indirect.

When worms crawl on an agar surface, the undulating body follows the contours of the groove made by the head during forward movement, and the head follows the groove made by the body during backward movement (26). Thus, the posture of the animal can largely be estimated from the trajectory of the head.

First, we converted the {$x(t), y(t)$} position of the head ganglia into coordinates for locomotion, {($v(t), \omega(t)$}, corresponding to the forward velocity of the worm (μm/s) and the angular velocity of the head in the ventral direction (rad/s). Next, we propagated the translational and curving movements of the head into the translation and curvature of all points along the body using phase lags dependent on fractional distance from the head, projecting all measurements onto the 4-dimensional subspace of worm locomotory postures (called “eigenworms”) to predict the smoothly time-varying posture of the body(27, 28). We developed this algorithm (see **Methods**) to perform this estimation based on the two-dimensional trajectory of the head ganglia recorded by our tracking microscope. We verified the ability of our algorithm to correlate head coordinates with body posture using low magnification imaging (4x). Using exclusively the velocity of the head ganglia, we were able to reconstruct the posture of a worm at all points along a trajectory (**Fig. 2a** and **Supplementary Video 1**). The trajectory and posture of an animal that was reconstituted solely from high-resolution recordings (40x) is also shown (**Fig. 2b**).

To quantify the correctness of our algorithm, we tested it against an online repository of postural analysis of freely crawling worms (28). Plugging the time-varying position of a coordinate fixed to the location of the head along the body into our algorithm, we reconstructed the complete posture of the animal. We were then able to compare the reconstructed posture to the documented posture available on the online repository. We calculated correlation coefficients at each point along the body. Our algorithm does not capture the variance in the movements anterior to the head ganglia. This is expected because the high frequency exploratory movements of the worm’s nose are largely uncorrelated with the movements of the body. However, our algorithm effectively captures much of the variance of the rest of the worm body (**Fig. 2c**). Because the estimate provided by our algorithm is not perfect, it may not be useful for applications where fine postural information is required, but may be useful in studies of navigational behavior, for example, where strategies are largely based on motor decisions that originate within the head and can be inferred from the movements of the head (dorsal or ventral bending for steering, or forward and backward movement).

Semi-automated registration of individual nuclei in the moving head ganglia

As an animal crawls, the relative location of neurons will change, sometimes dramatically, over the course of image acquisition (**Supplementary Movie 2**). Without fiducial markers that capture this changing geometry, it is impossible to identify regions that correspond to signals from specific neurons. One clever solution was to confine the calcium sensor to neuronal nuclei, creating easy-to-track, bright markers that simultaneously report neuronal activity (16). However, this approach suffered from the low baseline fluorescence of ultrasensitive calcium sensors, which did not allow the 5 millisecond exposure time needed for fast feedback for automated tracking. We modified the approach by expressing a bright calcium insensitive red fluorescent protein in the nuclei and the ultrasensitive green fluorescent calcium indicator GCaMP6s in the cytoplasm using two different panneuronal promoters (**Methods**). The two color imaging system allows us to use nuclear RFP to track individual neurons while capturing the calcium dynamics at the soma; it also enables us to use the calcium insensitive channels to estimate and mitigate motion artifacts.

The first step in the analysis was to assign a unique index to each neuron based on the position of its nucleus within the constellation of nearby nuclei. This was accomplished using several reference frames, with the animal in a variety of postural conformations. The worm movement will distort the configuration of its constellation that is proportional, to a certain degree, to their distance from the neuron. We use a combination of geometric and image-registration algorithms to identify the constellation that best resembles the local fluorescence pattern around a nucleus of interest. This provided a simple and automated means of assigning an index to all cells in all image frames. Manual proofreading was applied to remove sporadic errors in index assignment (**Supplementary Methods**).

The performance of this index assignment strategy was evaluated by applying it to dewarp image volumes. After we assigned indexes and coordinates to each cell in different image volumes, we applied a local rigid transformation to minimize the difference of each neuron's coordinate with respect to its location in a fixed atlas. Sample images from a movie showing a strong ventral bend, straight posture, and a strong dorsal bend are shown alongside atlas registered images (**Fig. 2d)**, illustrating the ability of the algorithm to subtract distortions due to bending.

Once an index has been assigned to a neuron in every image volume, its somatic calcium dynamics can be extracted from fluorescence in the red and green channels (**Fig. 3a**).

Classification and correlation of intracellular calcium dynamics with behaviors

Following this image analysis pipeline, we acquired calcium traces from 84 nuclear regions over the course of 216 seconds of recording of a moving worm that was subjected to a sinusoidal temperature fluctuation **(Fig. 2b)**. Our goal was to determine whether our setup was capable of finding distinct

neuronal activity patterns that correspond to sensory input and motor output. To activate the circuits for thermotaxis in *C. elegans,* which are most sensitive at temperatures near and above the temperature of cultivation, we cultivated worms at 15 °C and subjected them to fluctuations between 15 °C and 17.5 °C (3, 29). To extract general patterns in calcium dynamics across the head ganglia, we performed cluster analysis. Agglomerative hierarchical clustering was performed on the matrix of neural activity traces using the Pearson correlation coefficient as a distance measure. A linkage function (MATLAB) was applied to classify these traces into distinct clusters, and indexes were sorted to reflect this clustering (**Fig. 3b**). Correlated activity patterns within each cluster were evident in a cross-correlation matrix. Interestingly we found that the two largest clusters (denoted red and green in the cluster tree) exhibit anti-correlated activity patterns.

We selected the neurons with the strongest signal within the two largest clusters (4 for the green cluster, 7 for the red cluster) and compared their calcium dynamics with behavior (**Fig. 3c**). Neuron 4 exhibited an increase in activity during forward movement and a decrease in activity during backward movement. Neuron 7 exhibited the opposite correlation with directionality. We illustrate the overall distribution of indexed neurons that are positively and negatively correlated with directional movement across the head ganglia in **Fig. 3e**.

None of the main clusters exhibited activity patterns that correlated with the sinusoidal variation in ambient temperature. This is not due to a failure to sense temperature. We systematically searched the activity traces of all neurons, and identified two that were strongly correlated with thermosensory input (neurons 32 and 69) (**Fig. 3d,e**). The fact that the calcium dynamics of most neurons in the nerve ring encode motor output is supported by principal component analysis (**Fig. 3d**). We used the covariance matrix of neuronal activity patterns to calculate their principal components. The first two principal components, which encoded 54% of the total variance in brainwide neuronal dynamics, appear to be representations of worm directionality. The third principal component, which encoded 9%, represented the angular displacement of the head.

Assigning neuronal identities to indexed nuclei

Unambiguous identification of the neuronal identity is essential for interpreting their activity patterns. Lineage tracing using differential interference contrast (DIC) microscopy has shown that most cells (i.e. neuronal somas) in *C. elegans* are found in reproducible relative positions (30, 31). Assuming stereotypy, each automatically assigned index should correspond to a unique neuron. But for neurons that could have variable positions, the same cell may be assigned a different index in different animals. We asked whether our analyses can uncover activity patterns of specific cells with stereotyped locations by performing panneuronal recording and subsequent image analyses in three additional crawling worms (**Fig. 4a,b**). Across all four animals, indexes 32 and 69 were assigned to two neurons that responded to

temperature changes. Indexes 2, 6, 7, 28, and 49 were assigned to neurons that were activated by backward movement in all animals. Indexes 4 and 11 were assigned to neurons that were deactivated by backward movement. Because all index assignments were made blind to calcium dynamics, this result highlights the consistency of activity patterns and neuronal location across animals. To demonstrate the fraction of our signal that may be due to noise from the acquisition and analysis procedure, we prepared a worm with GCaMP6s replaced by GFP and collected traces from moving animals studied in the same way (**Fig. 4b**). In control animals, no significant temperature or motion correlated signals were observed in any neurons.

We sought the identity of neurons that exhibited strong calcium signals with high stereotypy. The unique morphology of *C. elegans* neurons could be readily observed by DIC microscopy. By examining high-resolution DIC images of an adult animal from the panneuronal imaging strain, overlaid with the red and green fluorescence signals from the neuronal reporters, we were able to identify cells that correspond to the 9 most highly stereotyped signals across the four animals (**Supplementary Figure 1**). The two neurons correlated with temperature inputs across the animals were the AFD thermosensory neurons: both AFDL (index 32) and AFDR (index 69) are activated by warming and deactivated by cooling during a sinusoidal temperature variation, consistent with previous reports (**Fig. 4b**) (32). The neurons consistently encoding forward locomotion were the AVB (index 4) premotor interneuron and the RMEL (index 11) head motor neuron. The consistent backward coding neurons were the AIBR (index 49) interneuron, and the AVAL (index 7), AVDL (index 28), and RIML (index 2) premotor interneurons. All of these activity patterns were consistent with previous reports of their activity patterns in moving animals (1, 2, 6, 33-36). The activity traces of all segmented neurons in the animals that we studied are shown in **Supplementary Figure 2**. We note that most neurons identified were located on the left side of the animal, where we recorded the strongest signals because the four animals crawled on their right sides (**Fig. 3a**).

We only observed a representation of sensory input in two neurons, AFDL (index 32) and AFDR (index 69). We asked whether activity patterns of additional neurons that correlated to temperature might be found by eliminating movement altogether. To do this, we completely immobilized worms from our panneuronal imaging strains using microbeads (37). With immobilized neurons, the ability to segment activity is improved, so we can determine whether additional neurons with significant temperature correlated responses might have escaped our analysis in moving worms. We calculated the correlation coefficient of each neuronal trace throughout the nerve ring of immobilized animals, and again found that the two neurons with the strongest temperature correlated responses were AFDL (index 32) and AFDR (index 69) (**Supplementary Figure 3**). In the immobilized worm, small but significant correlation was also found in two neurons in the anterior ganglion that we were unable to unambiguously identify. Nevertheless, these results support our conclusion that the representation of sensory input is largely localized to the AFD neurons.

Tracking thermosensory neurons in the crawling *Drosophila* larva

Single neuron tracking in moving *C. elegans* has been made tractable by the fact that their movement is largely restricted to two dimensions. It has not yet been possible to record calcium dynamics in other unrestrained animals such as *Drosophila* larva owing to their faster movements in all dimensions. Because *Drosophila* larva crawl using peristalsis waves, neurons undergo substantial Z-axis movements with each wave. When the larva picks a new direction during forward movement, it lifts and swings its head until it selects a new direction (38, 39). Because our system is capable of both three dimensional tracking and volumetric imaging, we asked whether it could meet the challenge of capturing calcium dynamics of neurons in the head of crawling *Drosophila* larva.

We recently discovered three thermosensory neurons in the dorsal organ of *Drosophila* larva that are required for positive thermotaxis up temperature gradients (23). Like the AFD neuron in *C. elegans,* they can phase-lock calcium dynamics to an oscillating thermosensory input (32). We used the *R11F02* Gal4 driver line to specifically target the express of both GCaMP6s and RFP in the cytosol of these sensory neurons, and monitored their calcium dynamics in a crawling larva subjected to sinusoidal temperature oscillations.

During a bout of spontaneous quiescence during the temperature cycle, we observed intracellular calcium signals that were characteristic of the sensory evoked response of the thermosensory neurons. During episodes of head swinging, where these neurons moved dramatically in an *xyz* trajectory, our system was able to track them within the image volume. We found identical calcium dynamics precisely phase-locked with temperature changes, as during the quiescence period. Therefore, the calcium dynamics of these sensory neurons is a representation of sensory input without significant correlation to movement (**Supplementary Figure 4**).

Discussion

Recent years have seen rapid development in multi-neuronal imaging systems in diverse preparations (13). A formidable challenge is to simultaneously observe brain-wide activity and behaviors of animals with defined sensory inputs, the only scenario where neuronal activity patterns can be properly correlated with sensory inputs and behavioral outputs. Our setup has uncovered patterns in sensorimotor transformation in the *C. elegans* nervous system that both buttress and extend recent findings from single or small number of neuron tracking in behaving animals, and brain-wide imaging in immobilized animals. The AFD neuron has been shown to be the dominant thermosensory neuron in *C. elegans,* required for all modes of thermotaxis (40, 41). While spontaneous activity in other sensory neurons have been shown to be modulated by temperature changes, only AFD phase locks its calcium dynamics to a rapidly

oscillating temperature waveform in a behaving animal (32, 42-44). Our recordings confirm that the thermosensory response is largely localized to AFDL and AFDR.

Brainwide imaging of unstimulated and immobilized worms has revealed spontaneous activity that are clustered into groups with correlated and anti-correlated patterns (16, 17). Neurons that exhibited activity increase during periods of backward movement by single neuron tracking in behaving animals (e.g., AIB, AVA) exhibited strongly correlated activity pattern in the panneuronal imaging setup in immobilized animals. Thus, periods of fictive forward or backward movement might be inferred from the activity patterns of different groups of neurons. The advantage of our system is the ability to make a direct correlation between brain dynamics and behavioral dynamics from sensory input to motor output.

A limitation of recording calcium dynamics in regions surrounding nuclei is that we are restricted to somatic calcium transients. Several neurons in *C. elegans* exhibit less calcium activity in their soma, with higher activity compartmentalized to their processes (5, 32, 45). Because processes of the head ganglia are tightly bundled fascicles, our current setup does not allow isolation of signals corresponding to individual neuronal processes. In these cases, sparse labeling of smaller groups of neurons is required to quantify their calcium dynamics. Our system may still be useful in these studies, however, as it would deliver a three dimensional recording of calcium dynamics throughout a cell, allowing comparison and contrast of calcium dynamics in different cellular compartments.

Our system now allows the extraction of correlations between neurons in the head ganglia, and their correlations with sensory input and motor output. Systematic analysis of brainwide activity patterns during complex behaviors like thermotaxis and chemotaxis may uncover characteristics in the information processing and decision-making process during the sensory to motor transformation. Comparison of brainwide activity patterns in animals with specific perturbations to the nervous system, e.g., by laser ablation or genetic inactivation of specific neurons, should reveal cellular and synaptic mechanisms for sensory to motor transformation.

Acknowledgments

We thank Andrew Leifer and members of the Samuel lab for useful discussions. This work was supported by an NSF Postdoctoral Fellowship and Burroughs Wellcome Award to VV, an NSF BRAIN EAGER Award to ADTS and grants from the NIH (1P01GM103770 and 8DP1GM105383-05). We thank D. Pilgrim for the P*rgef-1* promoter and O. Hobert for the panneuronal NLS-RFP strain.

Figure Legends

Figure 1. Experimental setup

(a) Microscopy schematic. Data was acquired using a spinning disk confocal microscope with red and green channels captured side-by-side on a CMOS sensor at 200 frames per second. A volume was imaged every 10 s using a piezo objective scanner. Every 20 frames were grouped together to form an image stack. Custom software controlled the stage and objective movements to maintain the tracked target at the center of the image volume.

(b) In all experiments, the animal was provided with a sinusoidal temperature stimulus using a custom thermoelectric stage (described in Klein et a., 2015). Temperature was recorded using a microthermocouple embedded at the agar surface.

Figure 2. Image processing for behavior and neuronal activity measurements.

(a) We verified the posture reconstruction algorithm by low-magnification (4x) tracking of a worm with the same transgenic line that we used in high magnification experiments. We used the trajectory of the animal's nerve ring The animal was completely visible, but we only used the trajectory of the animal's brain (information in the yellow box that would be available at 40x magnification) to compute its posture (green lines). The posture qualitatively fits a variety of complex configurations of the crawling worm, even those that are challenging to automatically segment using more conventional image-processing strategies such as omega turns when the head touches the tail. Trajectory represents 221 seconds of continuous recording starting from (s) and ending at (e).

(b) The computer posture and trajectory of an animal recorded at high magnification associated with the panneuronal imaging shown in Figure 3. The algorithm correctly predicts when the worm's tail will enter the field of view (red posture along the trajectory). Trajectory represents 121 seconds of continuous recording starting from (s) and ending at (e).

(c) By running the algorithm on published behavioral data for N2 worms freely crawling off of food, we can see the goodness of fit as a function of body coordinate (0 at head, 1 at tail). From the nerve ring (0.15 fractional distance from head) to the tail, the algorithm captures most of the variance of body posture.

(d) Effectiveness of automated identification of neuronal indexes during brainwide imaging is illustrated by dewarping the nerve ring using our registration algorithm (see **Methods**) that minimizes the displacement of the coordinates of all nuclei from a reference atlas. Three image volumes showing a deep ventral bend, deep dorsal bend, and straight posture from the worm recorded in Fig. 2b are shown. Also see **Supplementary Movies 1 & 2**.

Figure 3 Multineuronal activity patterns

(a) Images obtained in a 5 ms exposure with our setup in the red channel showing TagRFP and green channel showing cytosolic GCaMP6s. Each image is a slice through the acquired volume. Neurons are resolvable in the green channel, and nuclei are well resolved in the red channel in all dimensions. Signals are attenuated further from the objective.

(b) Normalized calcium dynamics of 84 neurons and matrix of correlation coefficients from the trajectory shown in Fig. 2b. Neuronal activity patterns are grouped and ordered by agglomerative hierarchical clustering. Neurons corresponding to the two largest clusters are highlighted in red and green on the tree diagram. Indexes corresponding to the neurons with the strongest signals within each cluster are indicated.

(c) Sample traces from a cell activated during forward movement (#7), a cell activated during backward movement (#4), and a cell correlated with temperature oscillations (#32).

(d) The first three principal components of the whole-brain neuronal activity correlate most strongly with behavioral output. The first two correlate with velocity, and the third component reports the angular velocity of the head.

(e) A volume showing the relative location of segmented neurons in one image volume. Neurons corresponding to the green and red clusters in Fig. 3b are colored accordingly. Neurons discussed in this figure along with Fig. 4 are annotated for reference. Two neurons correlated with thermosensory input are colored in blue. The position of the nerve ring is drawn for reference. The right side of the animal is into the page.

Figure 4 Stereotyped responses of indexed neurons.

(a) High-resolution stacks with simultaneous red (nucleus), green (cytoplasm), and DIC information were used to match the indexes with stereotyped activity patterns to their cellular identities (also see **Supplementary Figure 1**).

(b) Consistent signals across animals from temperature sensitive neurons (32-AFDL and 69-AFDR) and several neurons correlated with forward/backward movement, suggesting that the indexes assigned using DIC are the same as those recorded in roaming animals. Four worms (1-4) represent our standard imaging conditions with panneuronal GCaMP6s. The GFP control worm was subjected to the same imaging and analysis procedure, but using a transgenic worm that expressed panneuronal GFP. The residual signal in the control worm provides an estimate of total noise in the system caused by experimental measurement and the analysis pipeline.

Supplementary Figure 1. Neuronal identification in the nerve ring.

High-resolution image of an adult worm using differential interference contrast microscopy and confocal microscopy in the red and green channels using a Zeiss LSM 700 confocal system with an Axio Imager.Z2 microscope. Neurons that can be unambiguously identified based on cell morphology and

position corresponding to the indexes and calcium dynamics shown in **Fig. 4** are indicated in their sections. Optical sections were acquired with 1.16 micrometer Z-steps.

Supplementary Figure 2 Multineuronal activity patterns during thermosensory stimulation in moving *C. elegans*

Heatmaps (left panels) containing all extracted calcium dynamics for the five animals (worms 1-4, and GFP control) presented in Figure 4. We show calcium traces (right panels) for those neurons that we were able to reliably segment throughout each recording without gaps correlated with both thermosensory input and behavioral output. We extracted calcium traces from 84 neurons annotated for worm 1 (Supplementary Figure 2A), 31 for worm 2 (Supplementary Figure 2B), 82 for worm 3 (Supplementary Figure 2C), 26 for worm 4 (Supplementary Figure 2D), and 35 for the GFP-labeled control animal (Supplementary Figure 2E). We note the traces corresponding to the subset of identifiable neurons shown in Figure 4. Each set of traces is independently clustered for visualization.

Supplementary Figure 3. Temperature-correlated responses in immobilized worms.

In an animal completely immobilized with microbeads, we correlated the activity of 86 neurons with a temperature input that matched our freely moving conditions. The histogram of correlation coefficients reveals that the two neurons with the strongest correlation correspond to indexes 32 and 69, identified as AFDL and AFDR, respectively, in our experiments with roaming animals. Two unidentified neurons in the anterior ganglion (indexes 18 and 62) showed small but significant correlation. Data from two neurons, RMEL and AIBL, showed no correlation with temperature but, as expected, were anticorrelated; RME neurons are active during forward movement whereas AIB neurons are active during backward movement.

Supplementary Figure 4. Calcium activity in a moving *Drosophila* larva.

(a) Schematic of larval anatomy. Cold-sensing neurons of the dorsal organ ganglion are highlighted in green.

(b) Live images of the dorsal organ ganglia obtained during a tracking session. Images are maximum intensity projects along the x-, y-, and z-axes. The strain measured is *R11F02>GCaMP6s*.

(c) Left panels show calcium recordings during behavior in one mostly stationary animal (green) as well as three actively crawling animals (blue) correlated with temperature modulation. Right panels show trajectories in *xy* and *z* of the moving animal.

Supplementary movie 1: Reconstructing posture from a worm's head trajectory. A recording taken at 4x magnification of a worm freely navigating an agar surface. A 40x recording would only have access to information in the boxed yellow area. Using the trajectory of this region, we compute an estimate of the

animal's posture using a postural reconstruction algorithm (see text). The prediction is displayed in green, and closely matches the actual posture of crawling animal.

Supplementary movie 2: Raw whole-brain calcium recordings. Maximum intensity projections along the x, y, and z axes of a transgenic worm expressing GCaMP6s and nuclear RFP recordings under the control of panneuronal promoters. The data in Figures 2b and 3 are derived from this dataset.

Methods

Molecular Biology

GCamp6s was PCR amplified from pGP-CMV-GCaMP6s (Addgene) with BamHI and NotI restriction sites and subcloned in pCB101 behind the *rgef*-1 promoter (gift of D. Pilgrim) (20). We cultivated transgenic worms at 22 °C on nematode growth medium (NGM) plates with OP50 bacteria. zfIs124 was generated by injection of Prgef-1::GCaMP6s at 50 ng µl−1 into lin-15(n765ts) worms along with the lin-15 rescuing plasmid (pL15 EK) at 50 ng µl−1. The extrachromosomal array was integrated using gamma-ray irradiation and outcrossed four times to wild-type N2. Strain QW1217 was made by combining zfIs124 with otIs355(Prab-3::NLS::tagRFP) (gift of O. Hobert) (21). Strain QW1473 (rgef::GFP and rab3::NLS-tagRFP) was made by combining strain evIs111(Prgef::GFP;dpy-20) with otIs355(Prab-3::NLS::tagRFP) (46).

Behavioral measurements, microscopy hardware and software

The day before behavioral measurements, *C. elegans* were moved to a 15 °C incubator to ensure that their thermotactic setpoint was in a range that would generate a calcium signal in our experimental setup where we subjected animals to sinusoidal temperature waveforms between 15 and 17.5 °C. *Drosophila* larvae were cultivated and handled as described recently before being introduced to the experimental setup (23).

The setup is built around a Nikon Eclipse LV100 upright microscope. We imaged worms using a 4x, 0.2 numerical aperture (NA) Nikon Plan Apo objective (**Fig. 2A**) or the nerve ring at high resolution using a 40x, 0.95 NA Nikon Plan Apo Lambda objective. Worms were placed on 3 mm thick 2% agar surfaces and covered with a 48 mm x 65 mm #1 cover slip. We captured dual color images of a 115 µm x 115 µm field of view by projecting both images obtained using a Yokogawa CSU22 spinning disk confocal setup onto the sensor of an Andor Zyla 4.2 sCMOS camera using an Andor Optosplit II with an mCherry/GFP dichroic cube. The microscope stage was controlled by a Ludl BioPrecision2 XY motorized stage and MAC 6000 stage-controller, a PI P-721.LLQ high speed piezo, and a Ludl precision stepper motor with a linear encoder. During data acquisition, computer software kept the worm centered in the field of view via an automated feedback loop that provided real time image analysis and motion control. All data was collected with 4x4 binning and a vertically centered 256x512 pixel area of interest. The left half of this area consisted of the red output from the dichroic and the right half consisted of the green output. The measured pixel size of the system was 0.45 mm.

During acquisition, the camera provided the primary clock, running at 200 Hz, with one frame of data generated per clock cycle. Volumes consisted of 20 frames spaced 2 microns apart. The rastering triangular waveform was modified to optimally compensate for hysteresis due to the inertial load of the

microscope objective at these fast scanning rates. Optimal compensation was strongly objective dependent. Feedback in *xy* could occur after the acquisition and segmentation of each volume to find a bright centroid. However, feedback in *z* involved latency due to buffering of the voltage being output to the piezo. This resulted in a feedback time of roughly 0.5 seconds in typical operation. Image analysis and motion control were managed by custom software written in MATLAB, which was run in a Windows 7 environment with real-time priority. The code will be made freely available on www.github.com upon publication.

Postural reconstruction algorithm

Inputs:

$\hat{n}(t)$, the unit vector specifying the forward direction, evenly sampled

$\vec{x}(t)$, the trajectory of the nerve ring, sampled with $\hat{n}$

L , the length of the worm (in the same units as $\vec{x}$)

θ, an indicator of whether the worm is lying on its left or right side.

Output:

$P(t)$, an array of the estimated *x*- and *y*- coordinates for each of 100 segments

A worm's posture is stored as a series of 100 ordered pairs evenly spaced between the animal's nose and tail. The animal's head is assumed to be point 15. Whether the worm was lying on its left and right side was evident based on the ventral position of its vulva and the overall geometry of the nerve ring.

A worm's posture is reconstructed by storing the history of the worm's head's location on a stack (length-parametrized). When the worm moves forward, points are pushed to the stack. As it moves backwards, points are popped. To determine the posture at a given time, the top 0.85*L* of the stack is projected on to the nearest eigenworm (28).

To check for goodness of fit, we downloaded data from an online database corresponding to N2 worms grown off food (26 animals, up to 15 minutes per animal) (28). Worms were split into 100 segments, and angles between neighboring segments were calculated. The variation explained in **Fig. 2c** is the square of the Pearson correlation coefficient between predicted and "true" angles.

Identifying nuclear positions

Nuclei in the red imaging channel were tracked using a combination of manual annotation and standard image registration techniques. The processing pipeline was as follows:

1. Separate red and green volumes from each frame. Identify sporadic bad image volumes using coarse image statistics. Rotate and crop volumes to a standard size centered on the nerve ring using maximum intensity projections from the red and green channels.

2. Assign consistent indexes to nuclei in one or more reference frames. To obtain consistent indices across animals, we manually compared images between a registered index-labeled library and the unlabeled data set being analyzed. When neurons are in stereotyped positions, each index would thus be uniquely assigned to a specific cell type.

3. Select a nucleus for registration (the **active nucleus**). We want to ensure that frames are aligned to similar frames, and we want to avoid long-range error propagation. Registering frames sequentially in time can result in poor reference frame choices when the worm is moving dramatically. Often, we want to register a frame to a temporally distant but conformationally similar frame. Additionally, frames that are similar in the context of one nucleus may not be similar in the context of another due to long-range distortions through the animal's brain. This suggests that one should search for a different optimal registration order for each nucleus. To accomplish this, we used the following tree-based procedure for each active nucleus:

    a. Identify up to four nearby completely registered nuclei (**reference nuclei**).
    b. Using the coordinates of these reference nuclei, calculate a pairwise distance between frames as the L_1 norm of the differences of their coordinates. In the typical case of four reference nuclei, this would be the mean of the absolute values of 12 coordinate differences.
    c. Use these pairwise distances to generate a complete, weighted, undirected graph for the frames. Insert a dummy node into this graph with zero-weight connections only to the frames where the active nucleus has already been registered (either manually or from a previous iteration of the registration routine).
    d. Compute a minimum spanning tree for this graph rooted at the dummy node. By design, the children of the root node will be the previously registered frames.
    e. Perform a breadth-first search of the tree to generate the active nucleus's registration order along with a **reference frame** for each unregistered frame (parents in the registration tree).

4. Compute the location of the active nucleus in each frame (ordered as described above). Use the following method (steps e, f, and g are partly redundant, but they increase the robustness of the method):

a. Identify the coordinates of the reference nuclei in the current frame's reference frame.
b. Estimate a rigid transformation that will map the positions of the reference nuclei from the reference frame to the current frame.
c. Compare maximum-intensity projections in *x, y,*and *z* around a small volume centered around the preimage (in the reference frame) and image (in the current frame) of the transformation found in part b.
d. Perform pairwise image registration between the maximum intensity projections to obtain three transformations between the reference frame and the current frame.
e. Apply these transformations to the preimage coordinates of our active nucleus to obtain a new guess for its location in the current frame. The guesses for x and y are taken from the z-projection, the guess for z is the average of the values returned from the x and y projections.
f. Search for a bright point near the current guess and record its position. Gaussian masks are used to enforce an elastic penalty that keeps the chosen location near the current guess and away from previously registered nuclei.
g. Mark the nucleus as registered.

5. Perform proofreading to ensure that nuclei are correctly registered. Manual proofreading was performed for all neurons whose traces were reported in the main text (the 84 traces in **Fig. 3b** and the additional traces shown in **Fig. 4b**.

To visualize the quality of the locally rigid deformation that this algorithm implies (and identify regions that are being incorrectly warped), we can take several frames and fix their parent to some reference frame. Then we can apply our algorithm to each pixel in the original set of frames to see how the image is being deformed. This deformation is presented in **Fig. 2d**.

Extracting calcium dynamics

To extract signals, we first computed the mean pixel values *F(t)* in 2μm x 2μm x 4μm regions around each nucleus in the green channel. A slowly varying background $F_0(t)$ was computed and subtracted for each color channel to obtain the normalized signal: $f_g(t) = \frac{F(t)-F_0(t)}{F_0(t)}$. The same procedure was applied to the red channel to obtain $f_r(t)$. To mitigate motion artifacts that produce correlated signals between the red and green channels, we subtracted the correlated component between the red and green channels quantified by linear regression on a neuron-by-neuron basis. Pairwise similarity between neuronal signals was measured using Pearson correlation coefficients, and complete-linkage hierarchical clustering was performed with the resulting pairwise distances. Finally, principal components were calculated using the singular value decomposition method (without additional centering of data). We imaged worms for one to

three minutes each, and selected from each a 60 second interval to analyze in detail for calcium activity. This segment was selected on the basis of behavior such that it would include periods of both forward and reverse motion. No selection was made on calcium activity, and all extracted data is presented in **Supplementary Figure 2**.

References

1. Faumont S, et al. (2011) An image-free opto-mechanical system for creating virtual environments and imaging neuronal activity in freely moving Caenorhabditis elegans. *PLoS ONE* 6(9):e24666.

2. Kawano T, et al. (2011) An Imbalancing Act: Gap Junctions Reduce the Backward Motor Circuit Activity to Bias C. elegans for Forward Locomotion. *Neuron* 72(4):572–586.

3. Clark DA, et al. (2007) Temporal Activity Patterns in Thermosensory Neurons of Freely Moving Caenorhabditis elegans Encode Spatial Thermal Gradients. *Journal of Neuroscience* 27(23):6083–6090.

4. Suzuki H, et al. (2003) In Vivo Imaging of C. elegans Mechanosensory Neurons Demonstrates a Specific Role for the MEC-4 Channel in the Process of Gentle Touch Sensation. *Neuron* 39(6):1005–1017.

5. Chalasani SH, et al. (2007) Dissecting a circuit for olfactory behaviour in Caenorhabditis elegans. *Nature* 450(7166):63–70.

6. Piggott BJ, Liu J, Feng Z, Wescott SA, Xu XZS (2011) The Neural Circuits and Synaptic Mechanisms Underlying Motor Initiation in C. elegans. *Cell* 147(4):922–933.

7. Ahrens MB, et al. (2012) Brain-wide neuronal dynamics during motor adaptation in zebrafish. *Nature* 485(7399):471–477.

8. Flusberg BA, et al. (2008) High-speed, miniaturized fluorescence microscopy in freely moving mice. *Nature Methods* 5(11):935–938.

9. Katona G, et al. (2012) Fast two-photon in vivo imaging with three-dimensional random-access scanning in large tissue volumes. *Nature Methods* 9(2):201–208.

10. Holekamp TF, Turaga D, Holy TE (2008) Fast Three-Dimensional Fluorescence Imaging of Activity in Neural Populations by Objective-Coupled Planar Illumination Microscopy. *Neuron* 57(5):661–672.

11. Grewe BF, Langer D, Kasper H, Kampa BM, Helmchen F (2010) High-speed in vivo calcium imaging reveals neuronal network activity with near-millisecond precision. *Nature Methods* 7(5):399–405.

12. Cheng A, Gonçalves JT, Golshani P, Arisaka K, Portera-Cailliau C (2011) Simultaneous two-photon calcium imaging at different depths with spatiotemporal multiplexing. *Nature Methods* 8(2):139–142.

13. Deisseroth K, Schnitzer MJ (2013) Engineering approaches to illuminating brain structure and dynamics. *Neuron* 80(3):568–577.

14. Ziv Y, et al. (2013) Long-term dynamics of CA1 hippocampal place codes. *Nat Neurosci* 16(3):264–266.

15. Ahrens MB, Orger MB, Robson DN, Li JM, Keller PJ (2013) Whole-brain functional imaging at cellular resolution using light-sheet microscopy. *Nature Methods* 10(5):413–420.

16. Schrödel T, Prevedel R, Aumayr K, Zimmer M, Vaziri A (2013) Brain-wide 3D imaging of neuronal activity in Caenorhabditis elegans with sculpted light. *Nature Methods* 10(10):1013–1020.

17. Prevedel R, et al. (2014) Simultaneous whole-animal 3D imaging of neuronal activity using light-field microscopy. *Nature Methods* 11(7):727–730.

18. Abrahamsson S, et al. (2012) Fast multicolor 3D imaging using aberration-corrected multifocus microscopy. *Nature Methods* 10(1):60–63.

19. Kato S, et al. (2015) Global Brain Dynamics Embed the Motor Command Sequence of Caenorhabditis elegans. *Cell* 163(3):656–669.

20. Chen T-W, et al. (2013) Ultrasensitive fluorescent proteins for imaging neuronal activity. *Nature* 499(7458):295–300.

21. Tursun B, Patel T, Kratsios P, Hobert O (2011) Direct conversion of C. elegans germ cells into specific neuron types. *Science* 331(6015):304–308.

22. Nguyen JP, et al. (2015) Whole-brain calcium imaging with cellular resolution in freely behaving C. elegans. *arXiv* q-bio.NC.

23. Klein M, et al. (2015) Sensory determinants of behavioral dynamics in Drosophila thermotaxis. *Proc Natl Acad Sci USA* 112(2):E220–9.

24. Faumont S, Faumont S (2006) The Awake Behaving Worm: Simultaneous Imaging of Neuronal Activity and Behavior in Intact Animals at Millimeter Scale. *J Neurophysiol* 95(3):1976–1981.

25. Leifer AM, Fang-Yen C, Gershow M, Alkema MJ, Samuel ADT (2011) Optogenetic manipulation of neural activity in freely moving Caenorhabditis elegans. *Nature Methods* 8(2):147–152.

26. Gray J, Gray JM, Lissmann HW (1964) The Locomotion of Nematodes. *J Exp Biol* 41:135–154.

27. Stephens GJ, Johnson-Kerner B, Bialek W, Ryu WS (2008) Dimensionality and Dynamics in the Behavior of C. elegans. *PLoS Comput Biol* 4(4):e1000028.

28. Yemini E, Jucikas T, Grundy LJ, Brown AEX, Schafer WR (2013) A database of Caenorhabditis elegans behavioral phenotypes. *Nature Methods* 10(9):877–879.

29. Kimura KD, Miyawaki A, Matsumoto K, Mori I (2004) The C. elegans Thermosensory Neuron AFD Responds to Warming. *Current Biology* 14(14):1291–1295.

30. Sulston JE, Horvitz HR (1977) Post-embryonic cell lineages of the nematode, Caenorhabditis elegans. *Dev Biol* 56(1):110–156.

31. Sulston JE, Schierenberg E, White JG, Thomson JN (1983) The embryonic cell lineage of the nematode Caenorhabditis elegans. *Dev Biol* 100(1):64–119.

32. Clark DA, Clark DA (2006) The AFD Sensory Neurons Encode Multiple Functions Underlying Thermotactic Behavior in Caenorhabditis elegans. *Journal of Neuroscience* 26(28):7444–7451.

33. Ben Arous J, Tanizawa Y, Rabinowitch I, Chatenay D, Schafer WR (2010) Automated imaging of neuronal activity in freely behaving Caenorhabditis elegans. *J Neurosci Methods* 187(2):229–234.

34. Wen Q, et al. (2012) Proprioceptive Coupling within Motor Neurons Drives C. elegans Forward Locomotion. *Neuron* 76(4):750–761.

687 35. Chronis N, Zimmer M, Bargmann CI (2007) Microfluidics for in vivo imaging of neuronal and
688 behavioral activity in Caenorhabditis elegans. *Nature Methods* 4(9):727–731.

689 36. Guo ZV, Hart AC, Ramanathan S (2009) Optical interrogation of neural circuits in Caenorhabditis
690 elegans. *Nature Methods* 6(12):891–896.

691 37. Kim E, Sun L, Gabel CV, Fang-Yen C (2013) Long-Term Imaging of Caenorhabditis elegans Using
692 Nanoparticle-Mediated Immobilization. *PLoS ONE* 8(1):e53419.

693 38. Luo L, et al. (2010) Navigational decision making in Drosophila thermotaxis. *J Neurosci*
694 30(12):4261–4272.

695 39. Gomez-Marin A, Louis M (2012) Active sensation during orientation behavior in the Drosophila
696 larva: more sense than luck. *Curr Opin Neurobiol* 22(2):208–215.

697 40. Luo L, et al. (2014) Bidirectional thermotaxis in Caenorhabditis elegans is mediated by distinct
698 sensorimotor strategies driven by the AFD thermosensory neurons. *Proc Natl Acad Sci USA*
699 111(7):2776–2781.

700 41. Ohnishi N, Kuhara A, Nakamura F, Okochi Y, Mori I (2011) Bidirectional regulation of thermotaxis
701 by glutamate transmissions in Caenorhabditis elegans. *The EMBO Journal* 30(7):1376–1388.

702 42. Beverly M, Anbil S, Sengupta P, Sengupta P (2011) Degeneracy and Neuromodulation among
703 Thermosensory Neurons Contribute to Robust Thermosensory Behaviors in Caenorhabditis
704 elegans. *Journal of Neuroscience* 31(32):11718–11727.

705 43. Kuhara A, et al. (2008) Temperature Sensing by an Olfactory Neuron in a Circuit Controlling
706 Behavior of C. elegans. *Science* 320(5877):803–807.

707 44. Biron D, Wasserman S, Thomas JH, Samuel ADT, Sengupta P (2008) An olfactory neuron
708 responds stochastically to temperature and modulates Caenorhabditis elegans thermotactic
709 behavior. *Proc Natl Acad Sci USA* 105(31):11002–11007.

710 45. Hendricks M, Ha H-I, Maffey N, Zhang Y (2012) Compartmentalized calcium dynamics in a C.
711 elegans interneuron encode head movement. *Nature* 487(7405):99–103.

712 46. Altun-Gultekin Z, et al. (2001) A regulatory cascade of three homeobox genes, ceh-10, ttx-3 and
713 ceh-23, controls cell fate specification of a defined interneuron class in C. elegans. *Development*
714 128(11):1951–1969.

715

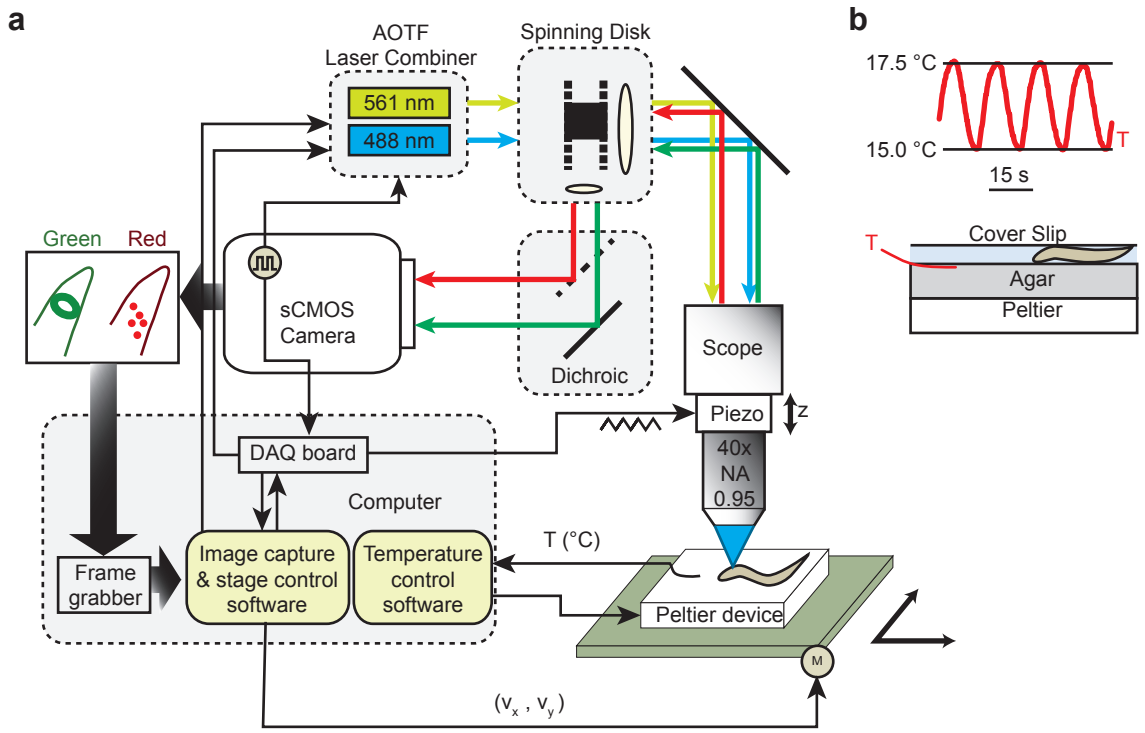
a
AOTF
Laser Combiner
561 nm
488 nm
Spinning Disk
Green
Red
sCMOS
Camera
Dichroic
Scope
Piezo
z
40x
NA
0.95
DAQ board
Computer
Frame
grabber
Image capture
& stage control
software
Temperature
control
software
T (°C)
Peltier device
M
(v_x , v_y)
b
17.5 °C
15.0 °C
T
15 s
Cover Slip
T
Agar
Peltier

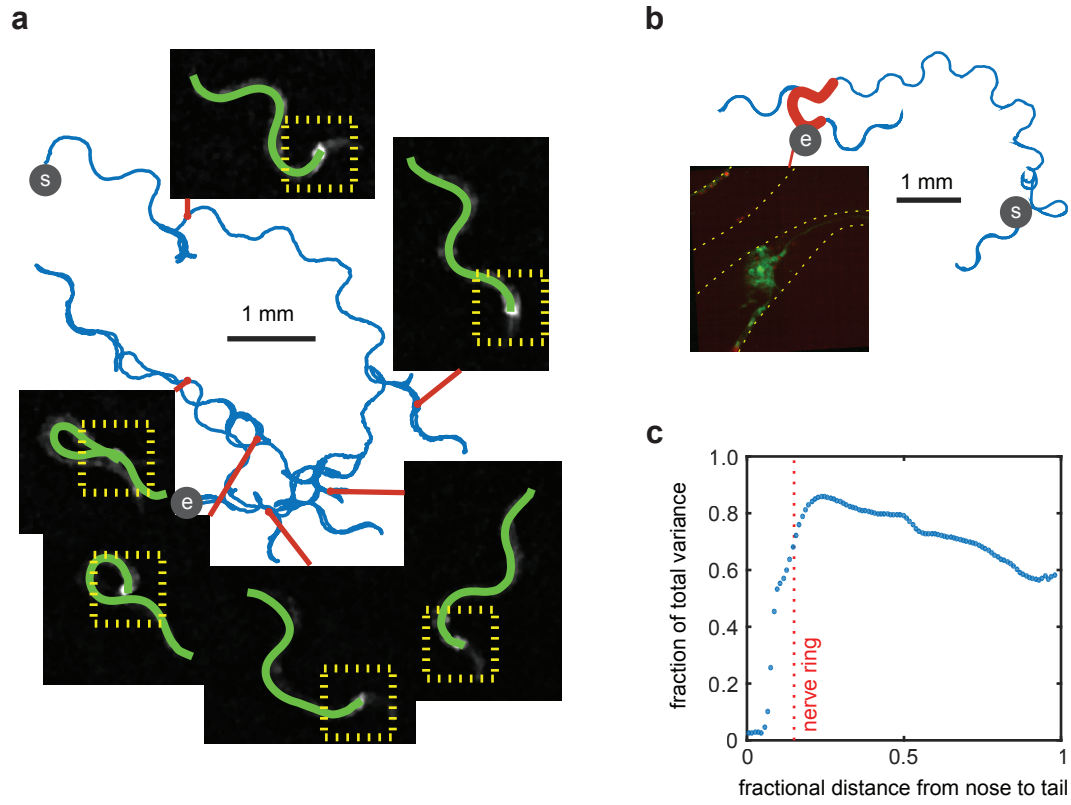
a
s
1 mm
e
b
e
1 mm
s
c
fraction of total variance
1.0
0.8
0.6
0.4
0.2
0
nerve ring
0
0.5
1
fractional distance from nose to tail
d
dewarping and registration

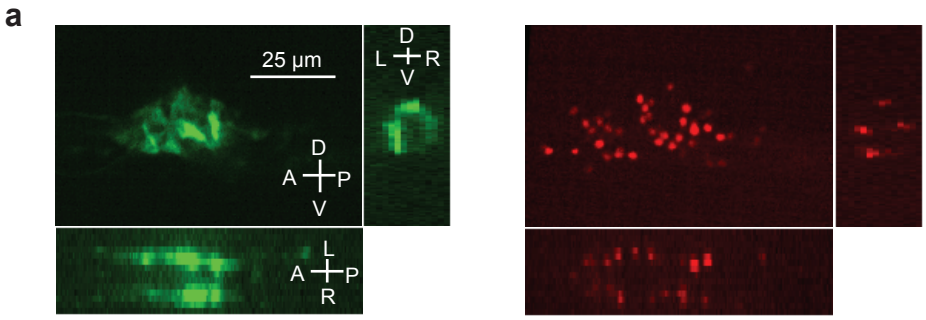
a
25 µm
D
L
R
V
D
A
P
V
L
A
P
R

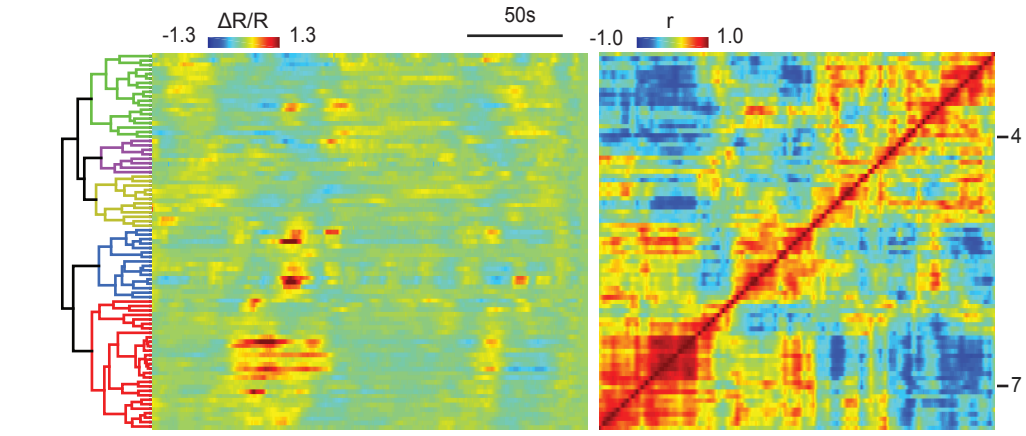
b
ΔR/R
-1.3
1.3
50s
r
-1.0
1.0
4
7

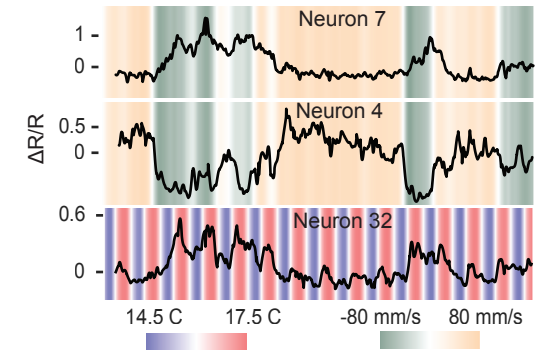
c
Neuron 7
1
0
Neuron 4
ΔR/R
0.5
0
Neuron 32
0.6
0
14.5 C
17.5 C
-80 mm/s
80 mm/s

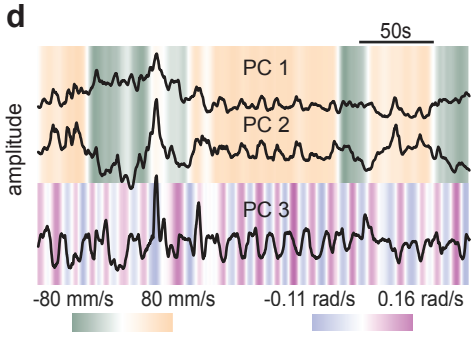
d
50s
PC 1
PC 2
amplitude
PC 3
-80 mm/s
80 mm/s
-0.11 rad/s
0.16 rad/s

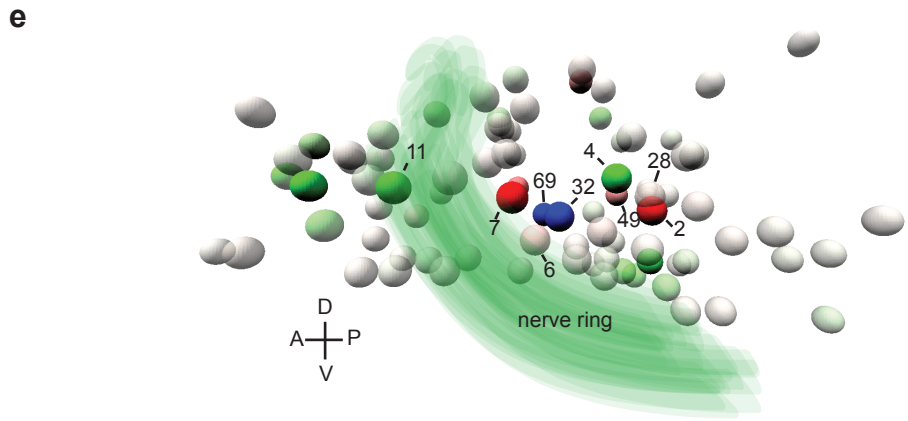
e
11
4
28
69
32
49
2
7
6
D
A
P
V
nerve ring

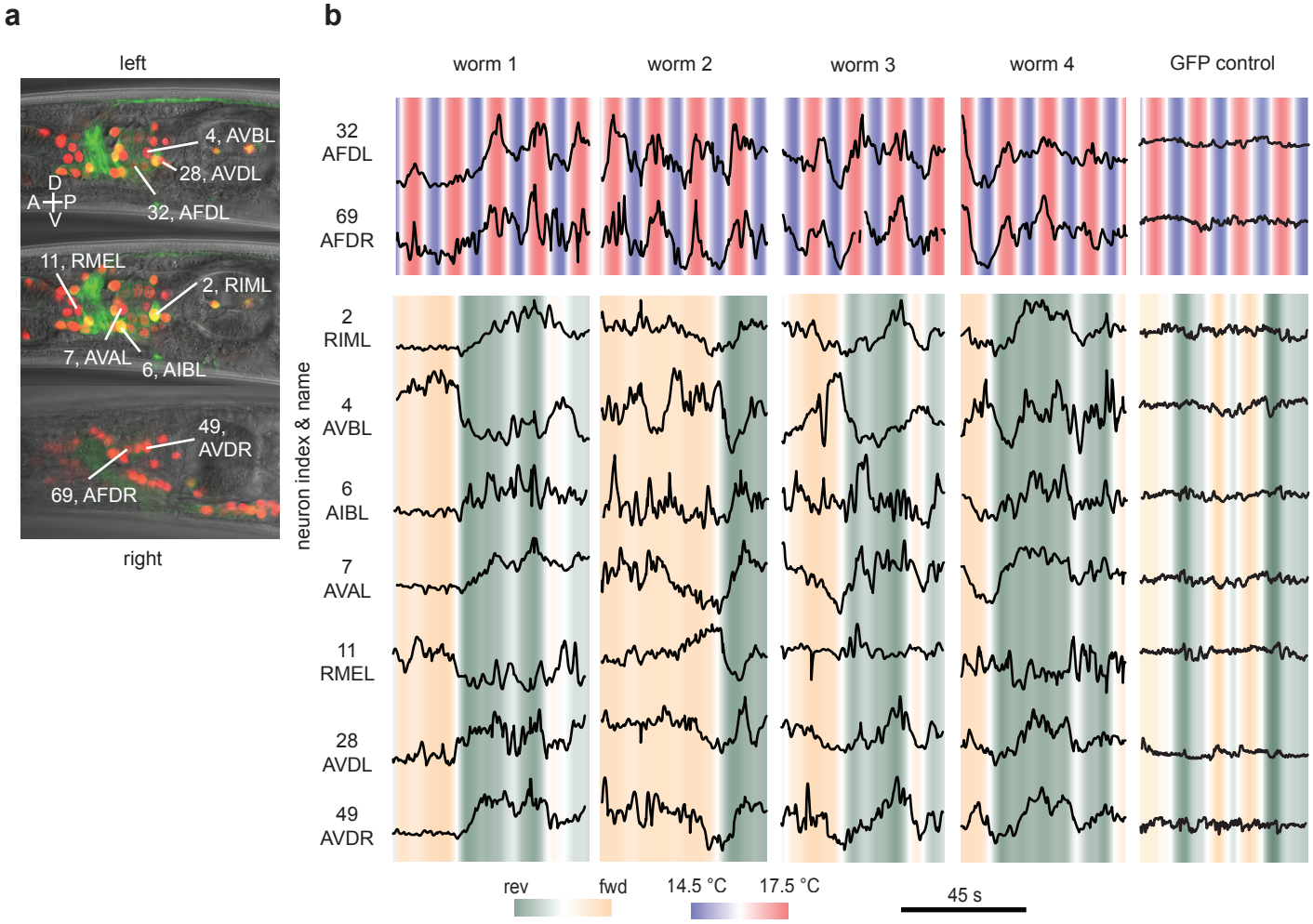
a
left
4, AVBL
28, AVDL
32, AFDL
D
A
P
V
11, RMEL
2, RIML
7, AVAL
6, AIBL
49,
AVDR
69, AFDR
right
b
worm 1
worm 2
worm 3
worm 4
GFP control
32
AFDL
69
AFDR
neuron index & name
2
RIML
4
AVBL
6
AIBL
7
AVAL
11
RMEL
28
AVDL
49
AVDR
rev
fwd
14.5 °C
17.5 °C
45 s

Slice 1

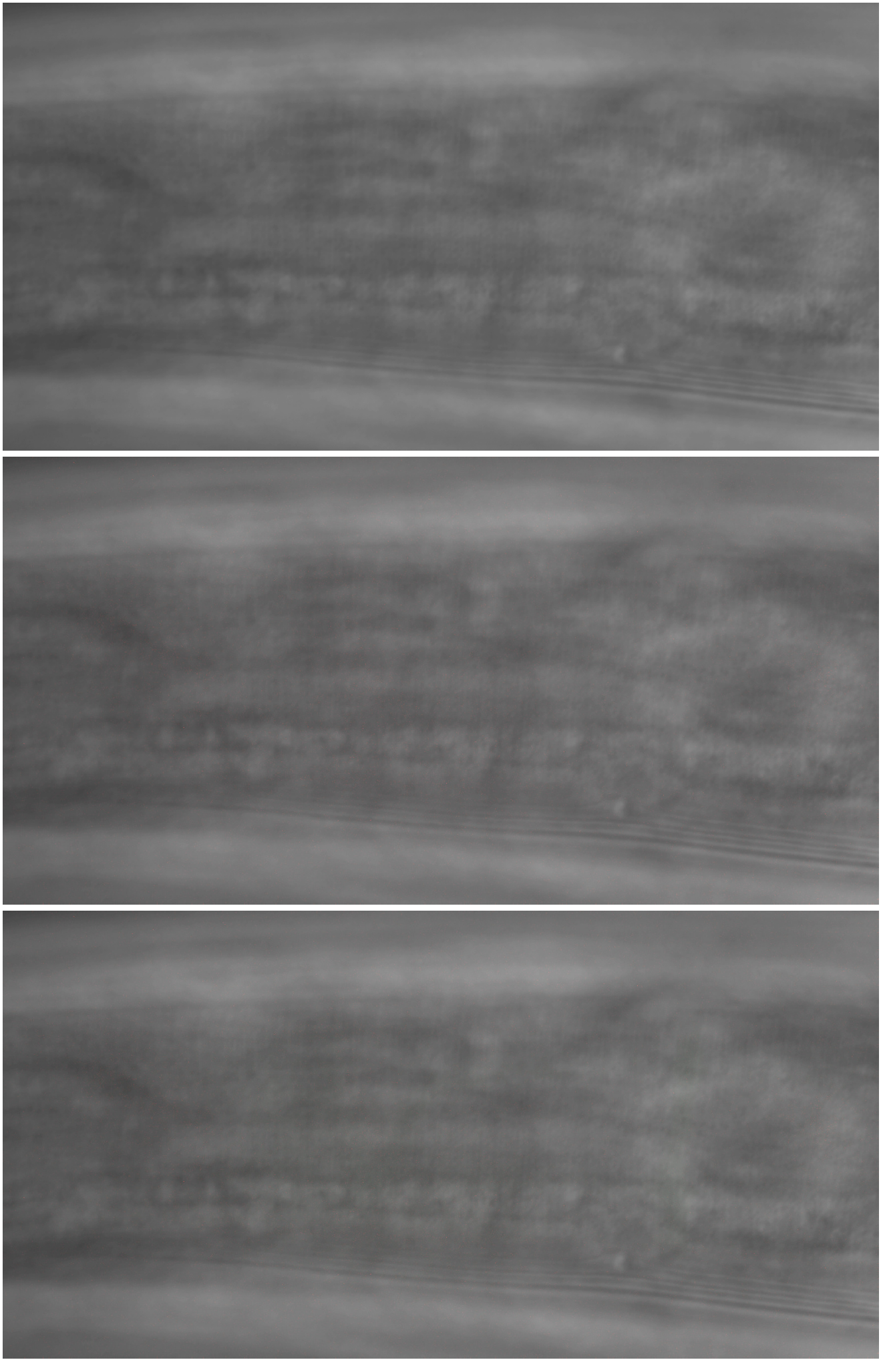

Slice 2

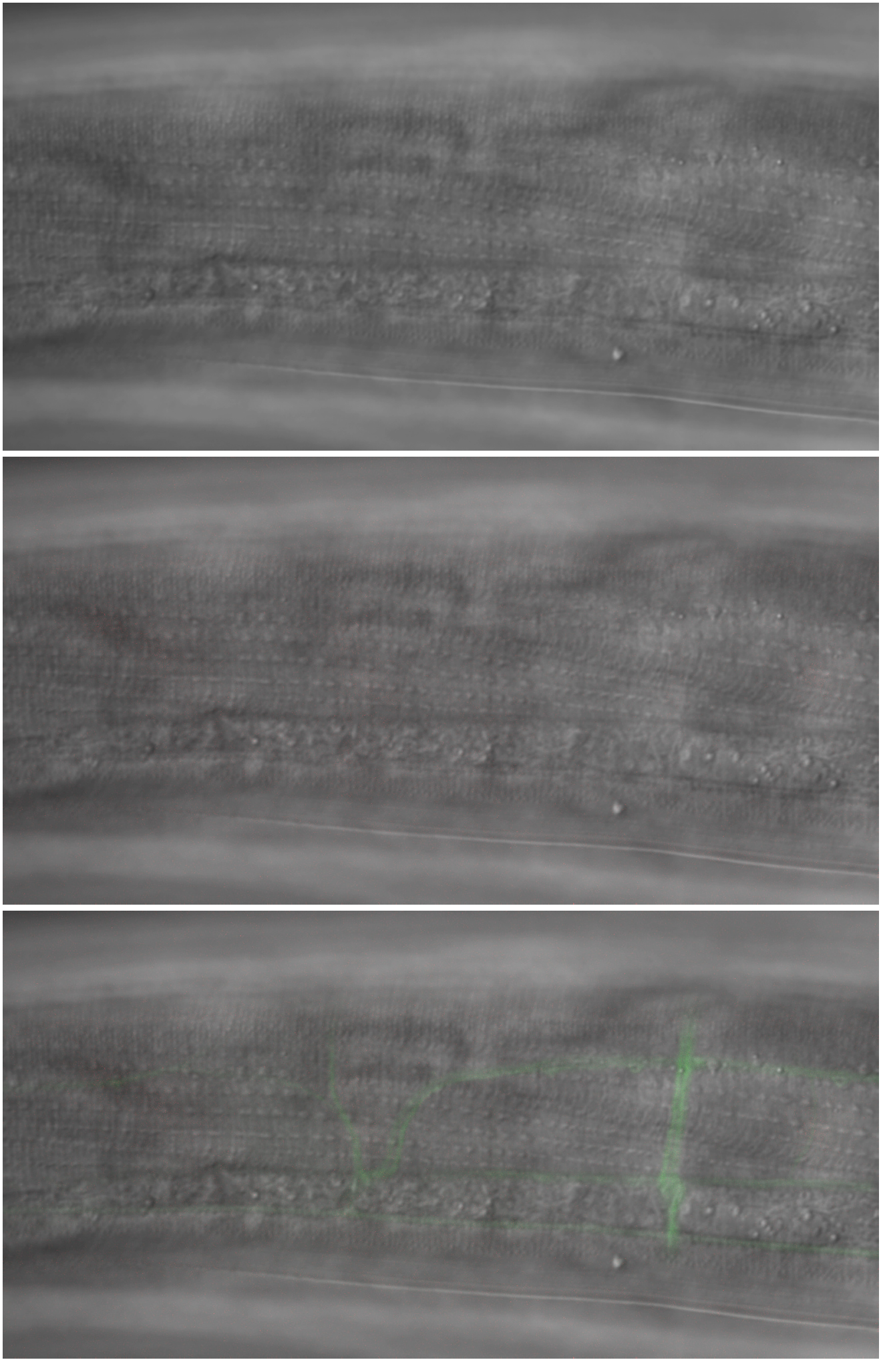

Slice 3

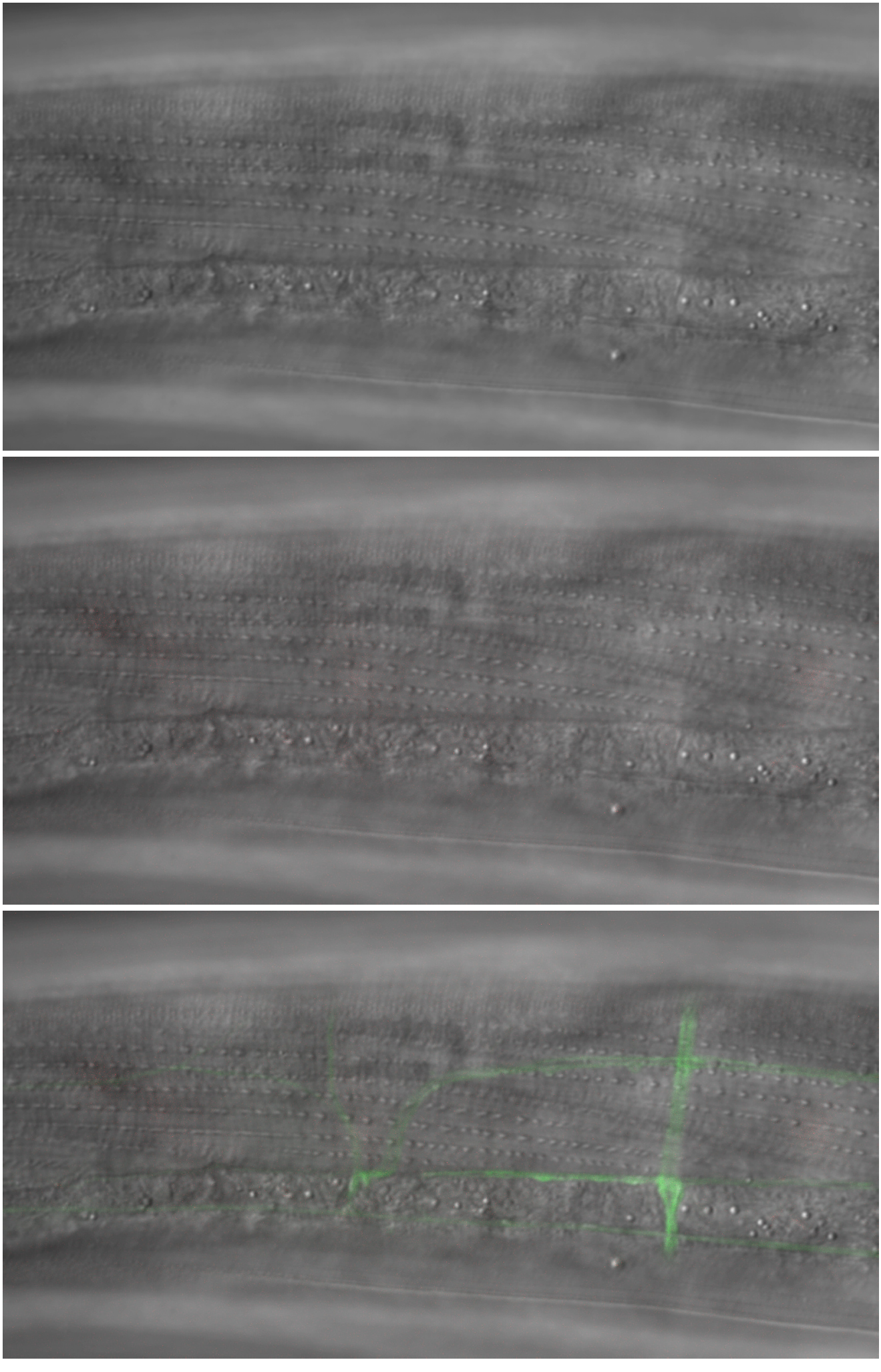

Slice 4

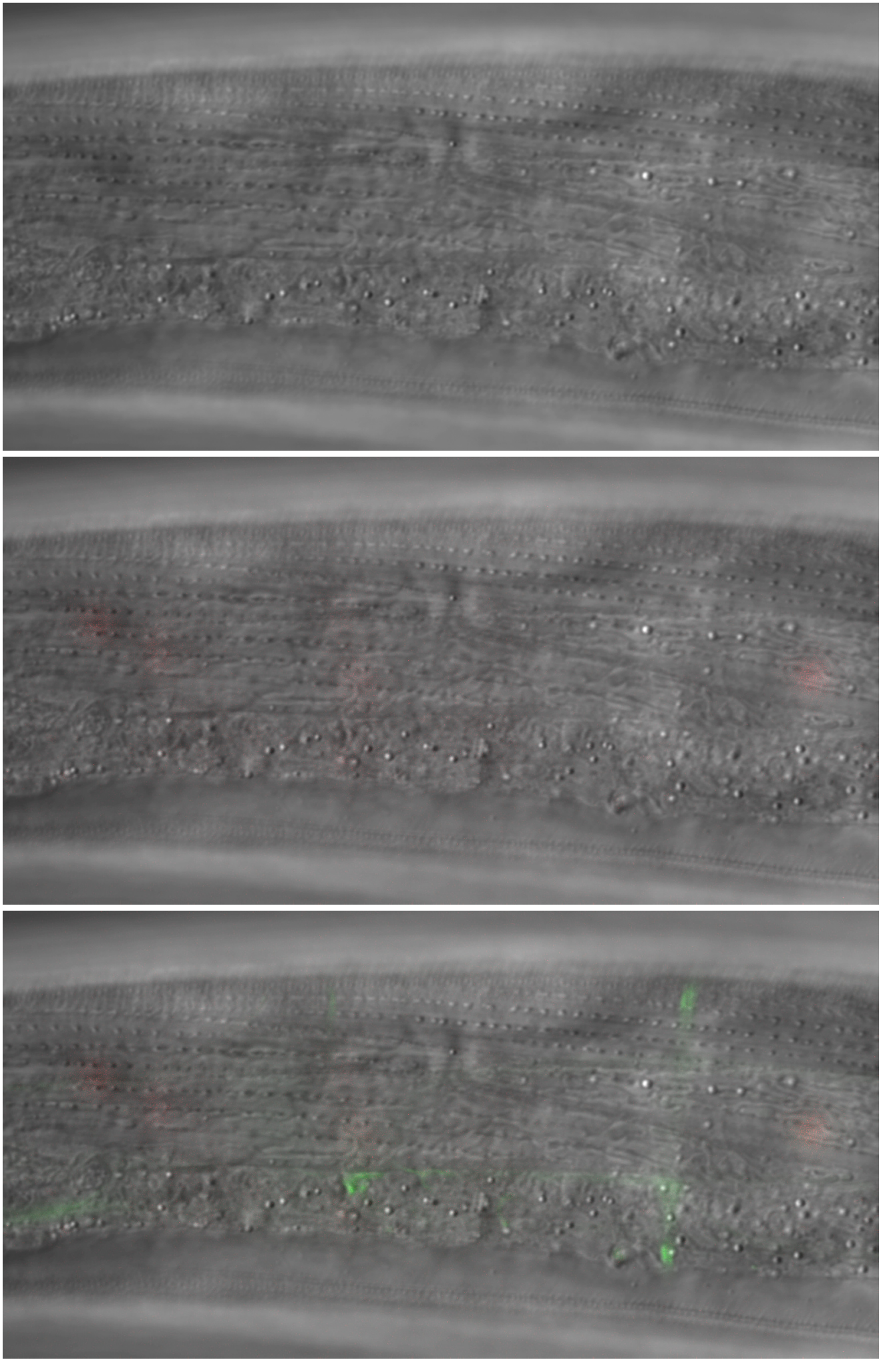

Slice 5

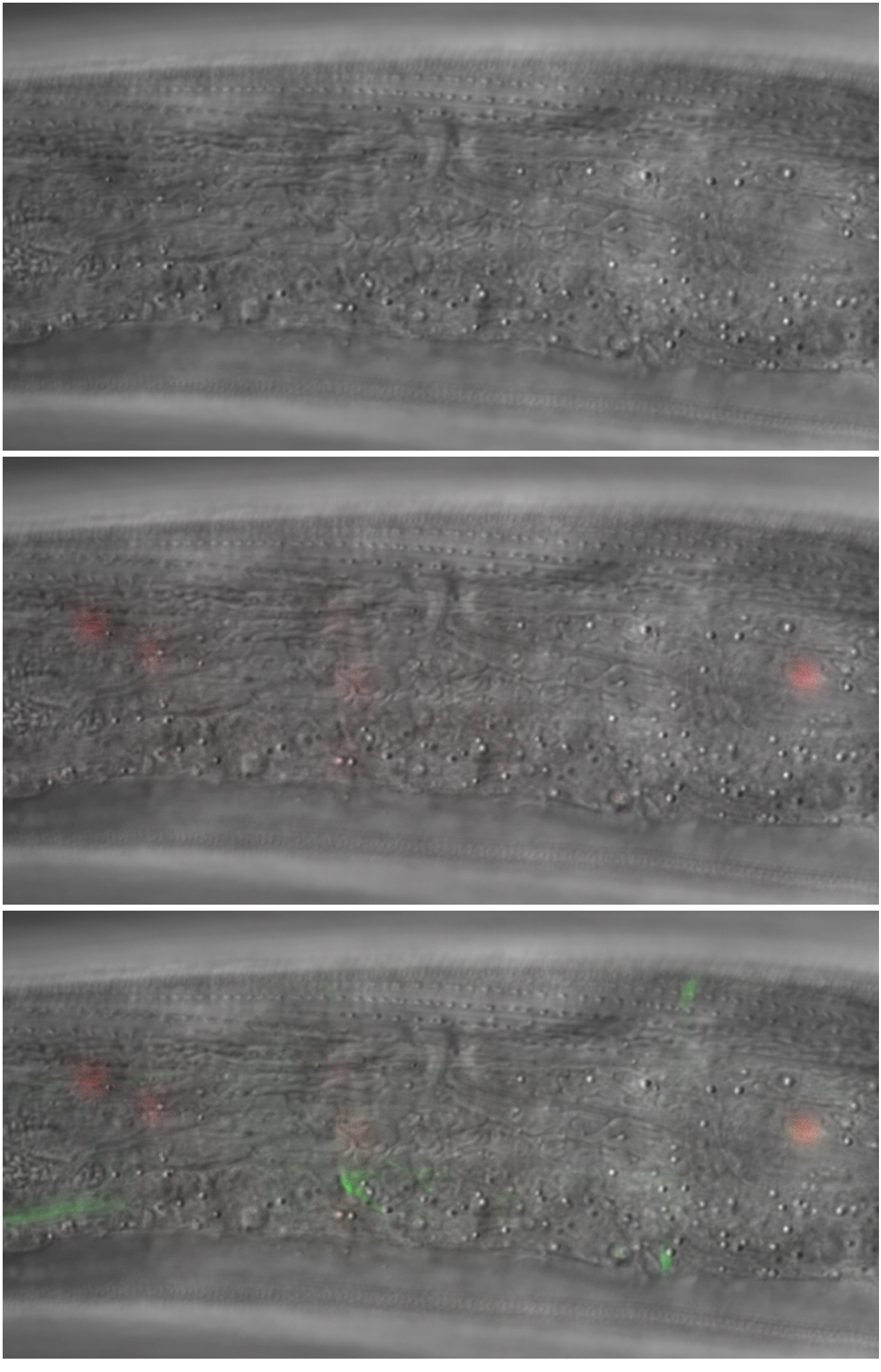

Slice 6

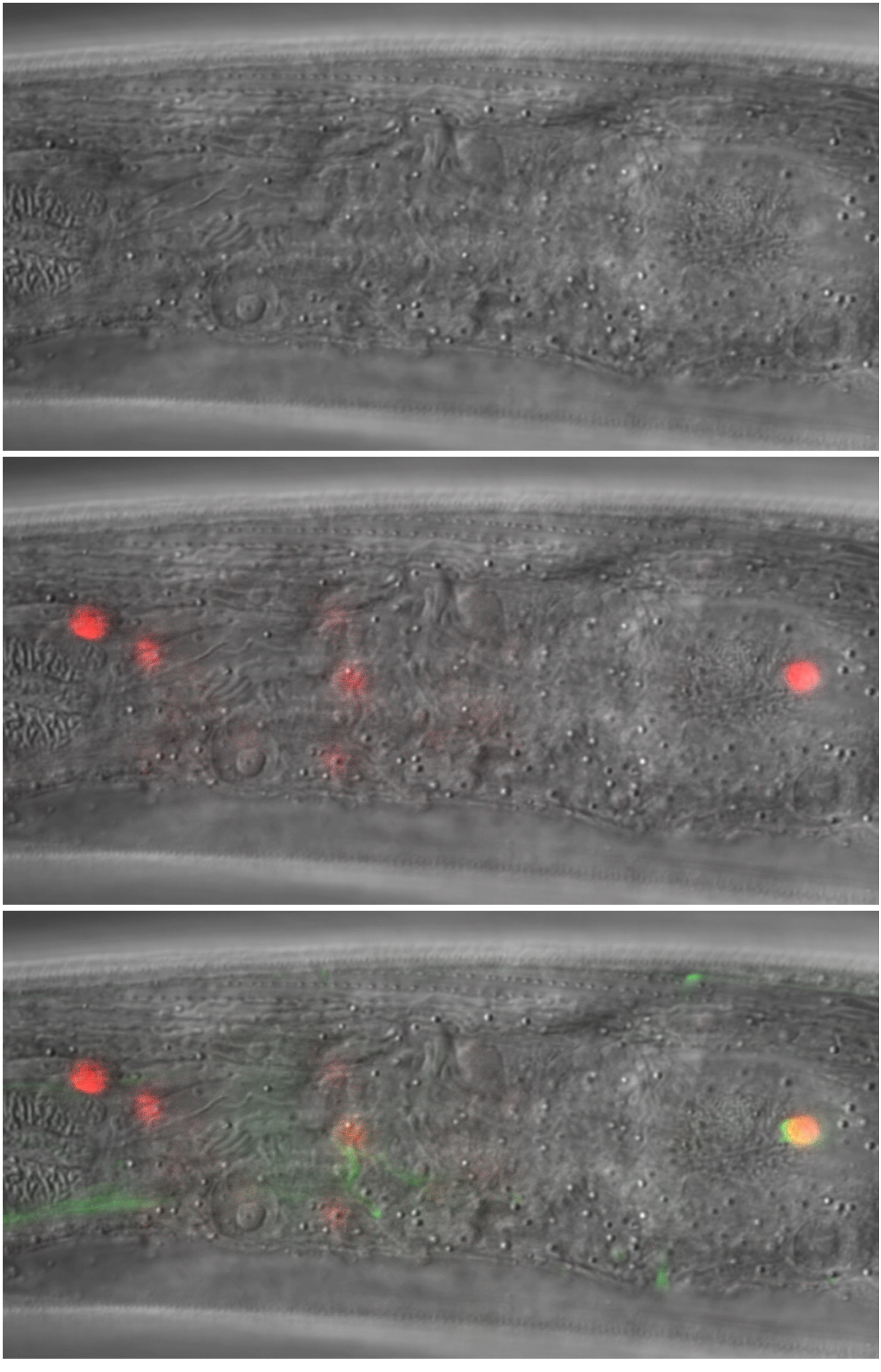

Slice 7

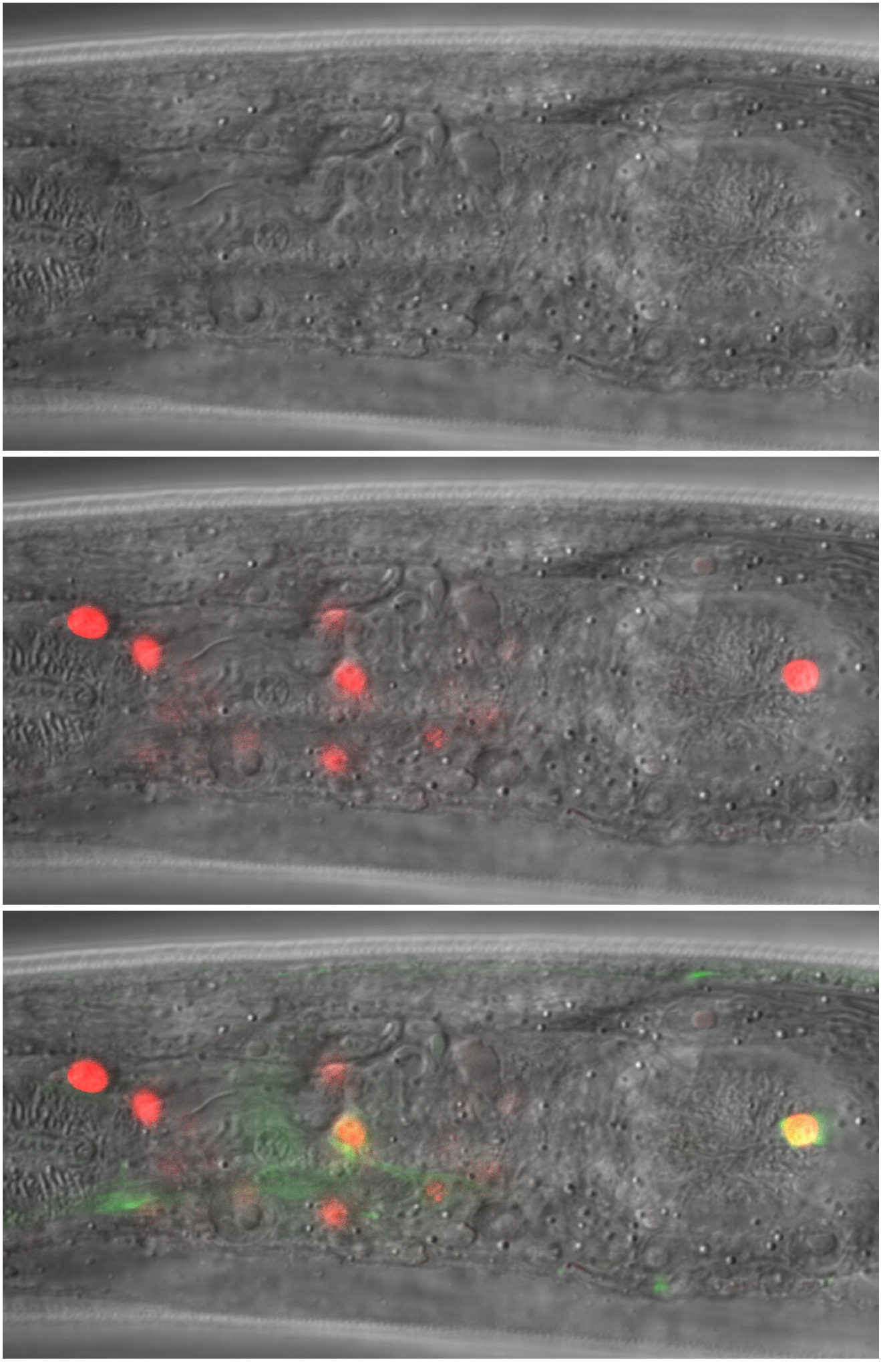

Slice 8

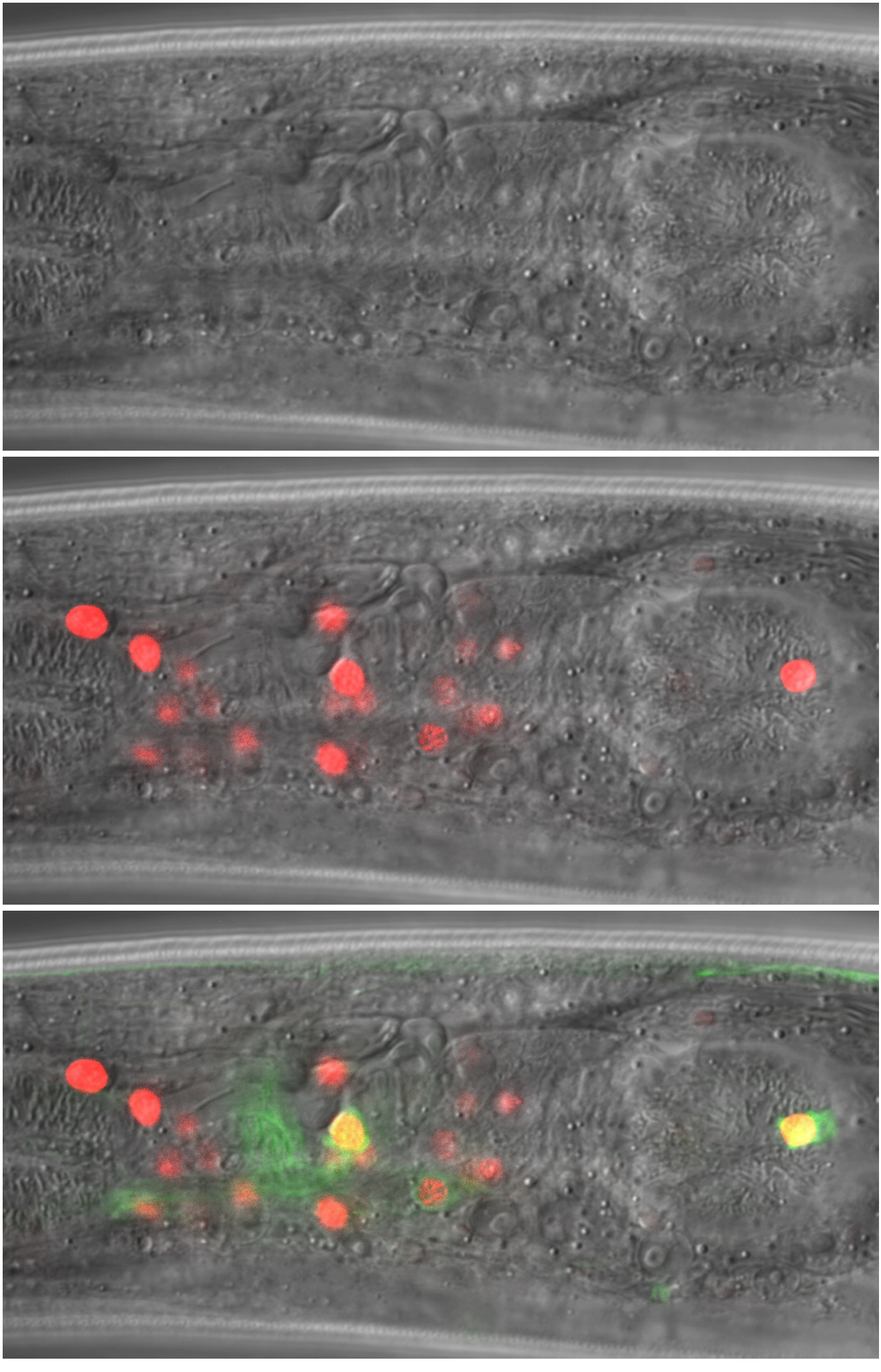

Slice 9

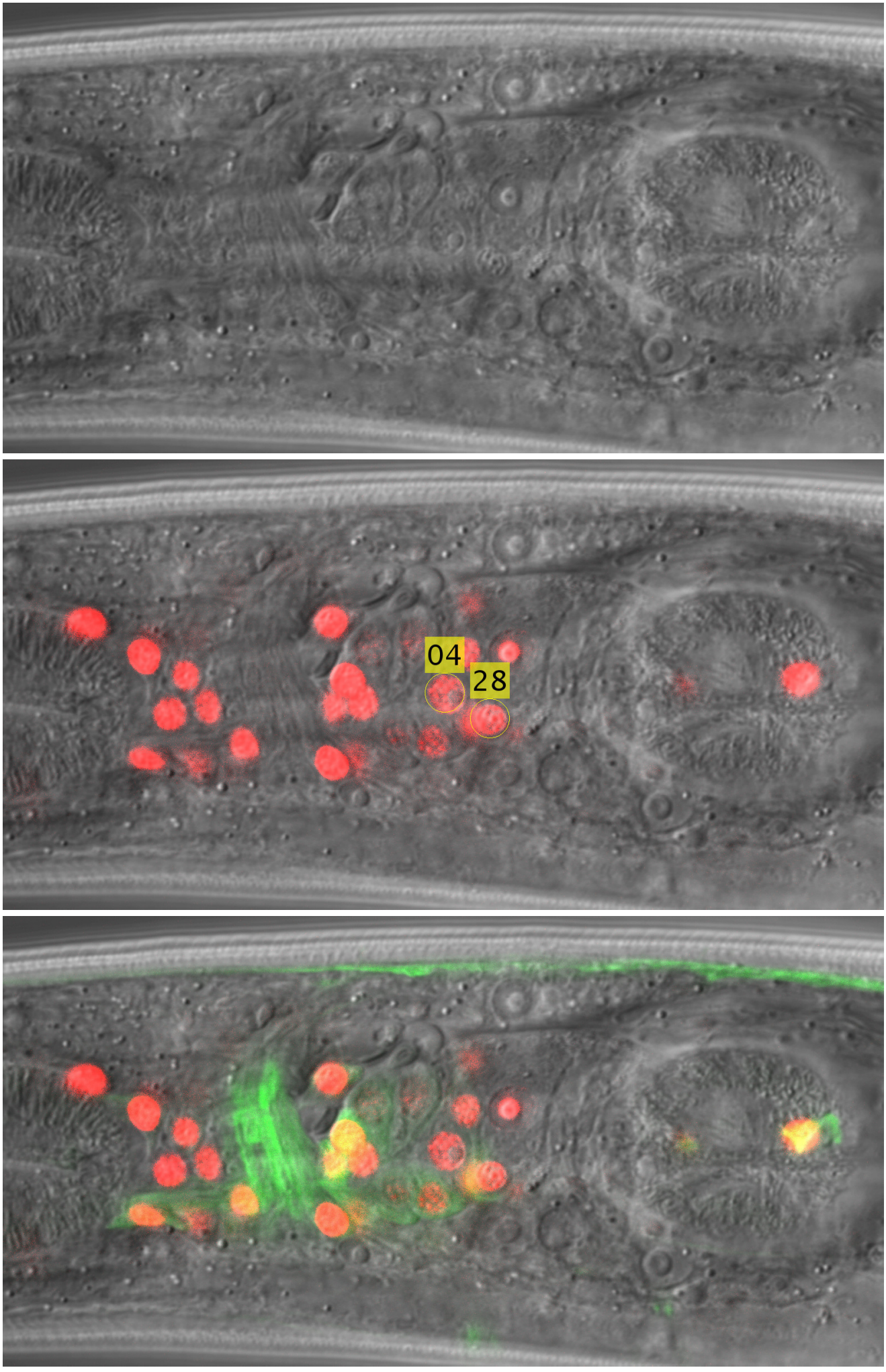

Slice 10

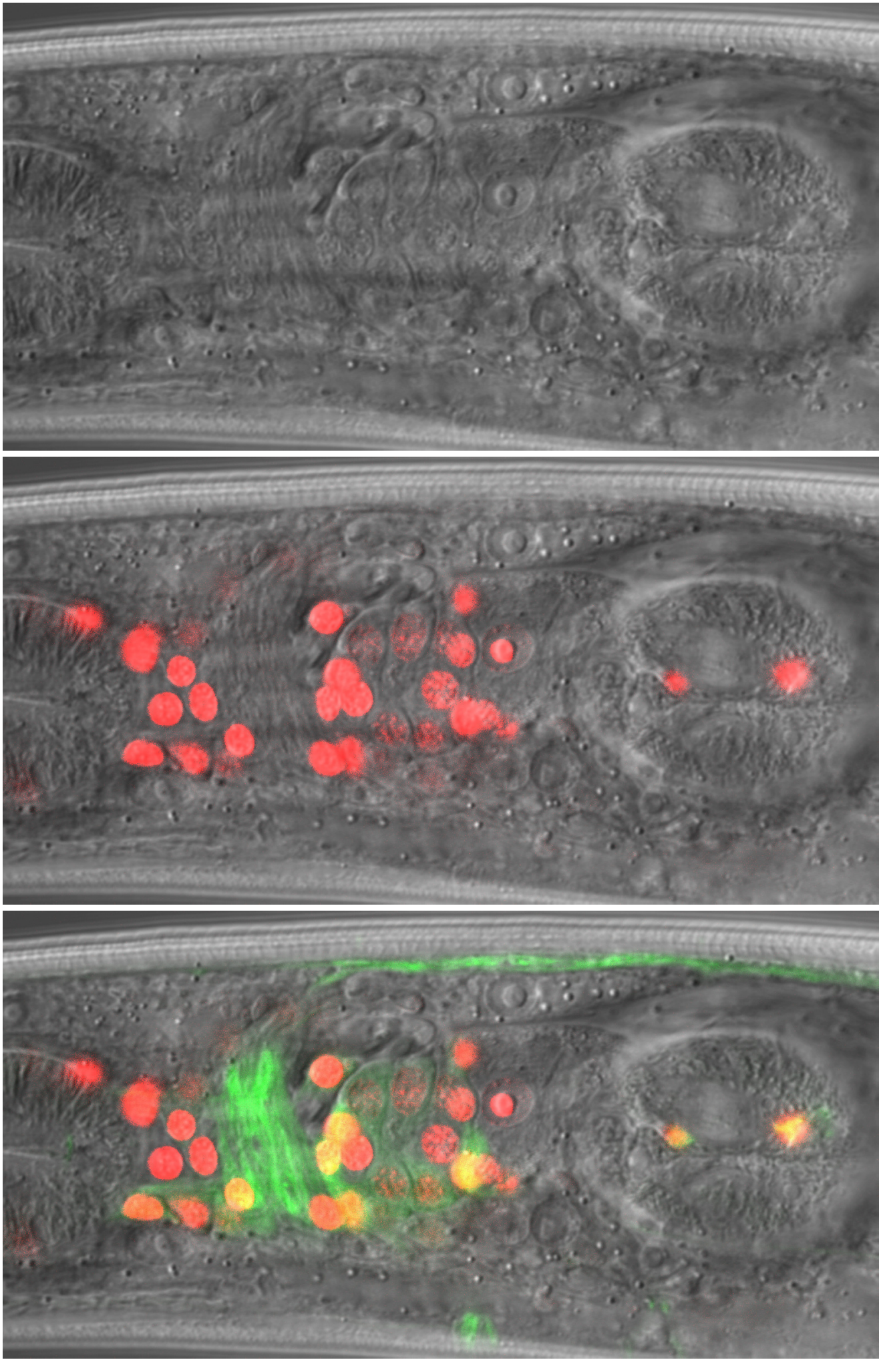

Slice 11

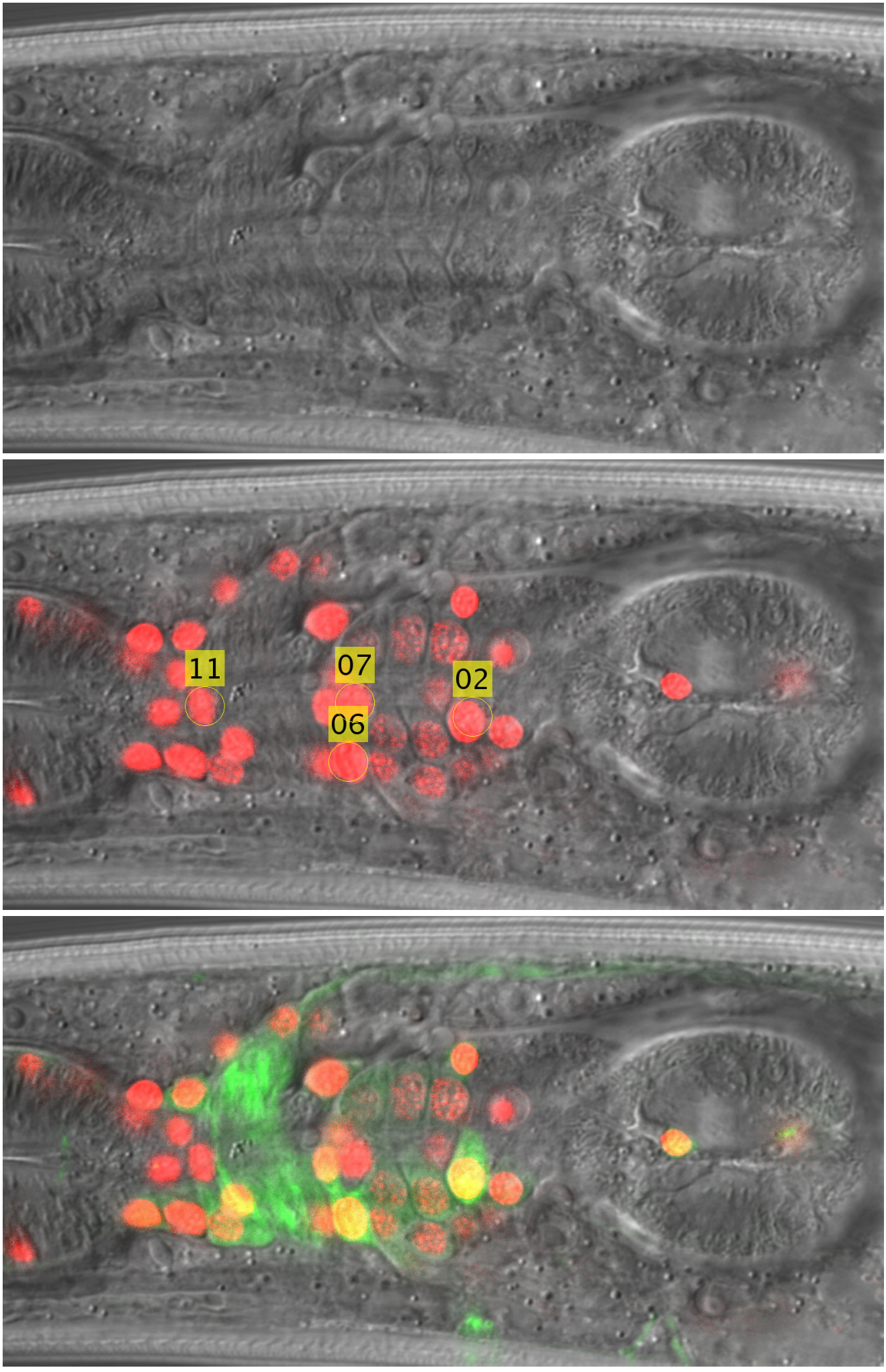

Slice 12

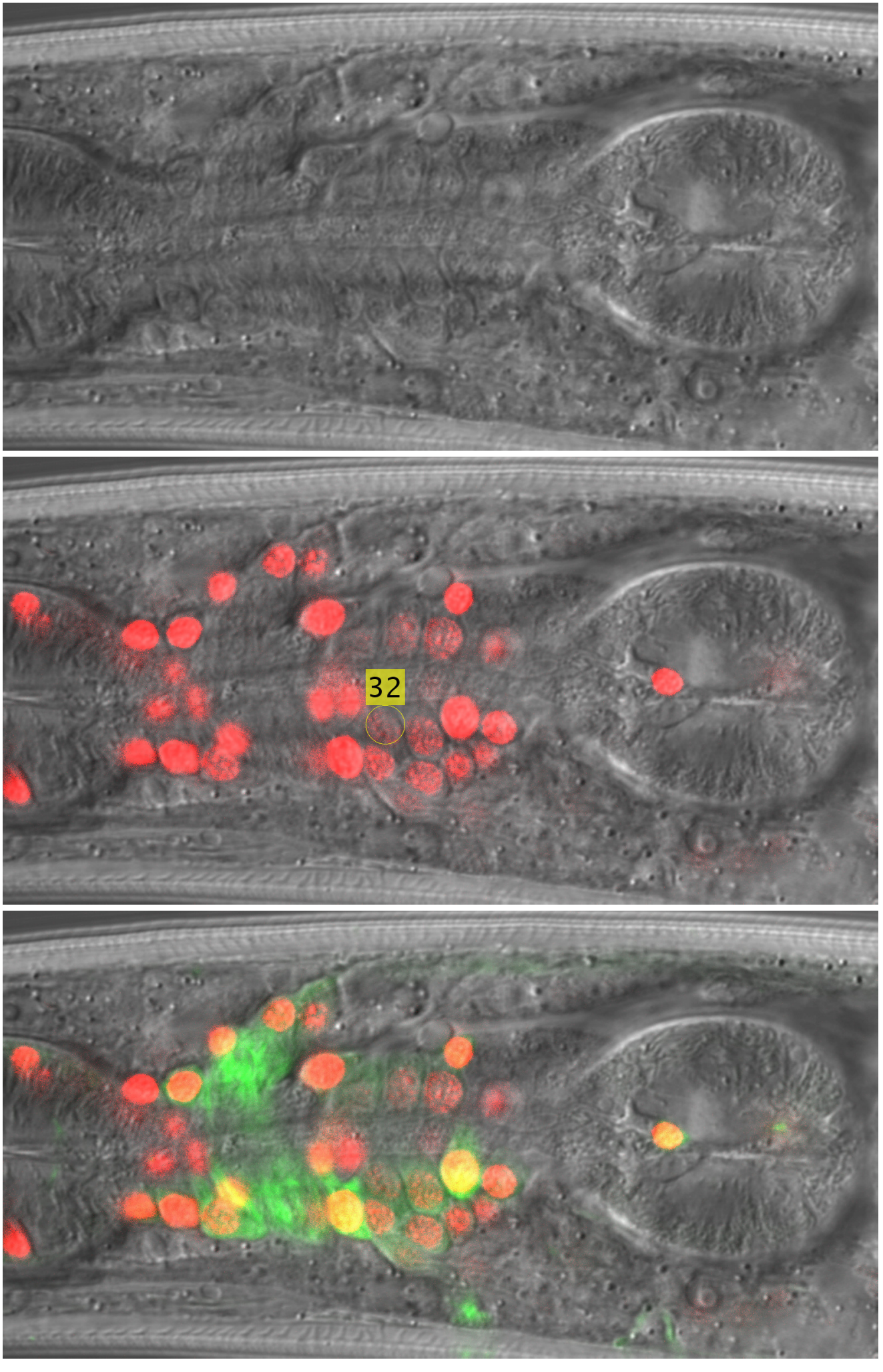

Slice 13

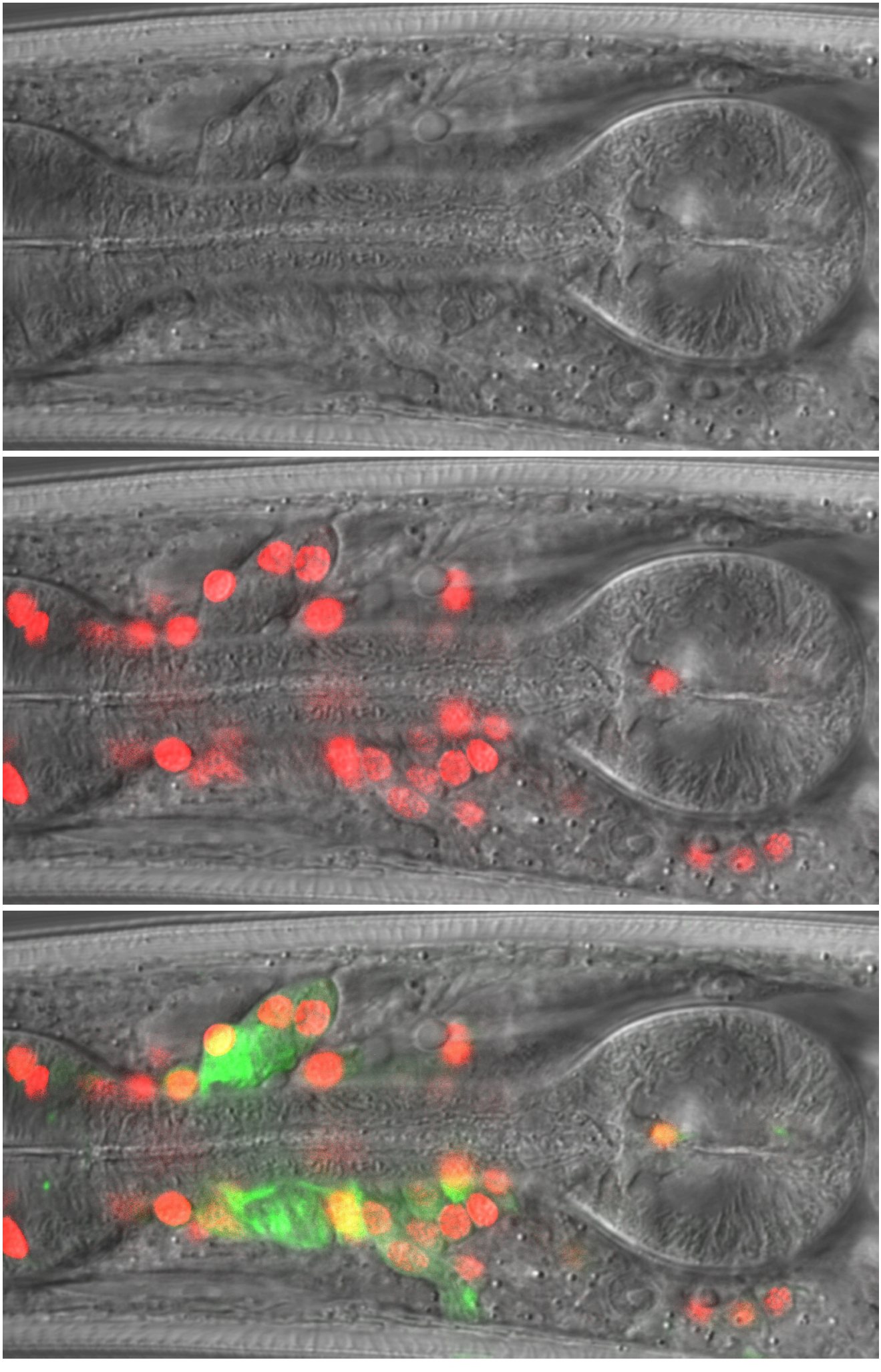

Slice 14

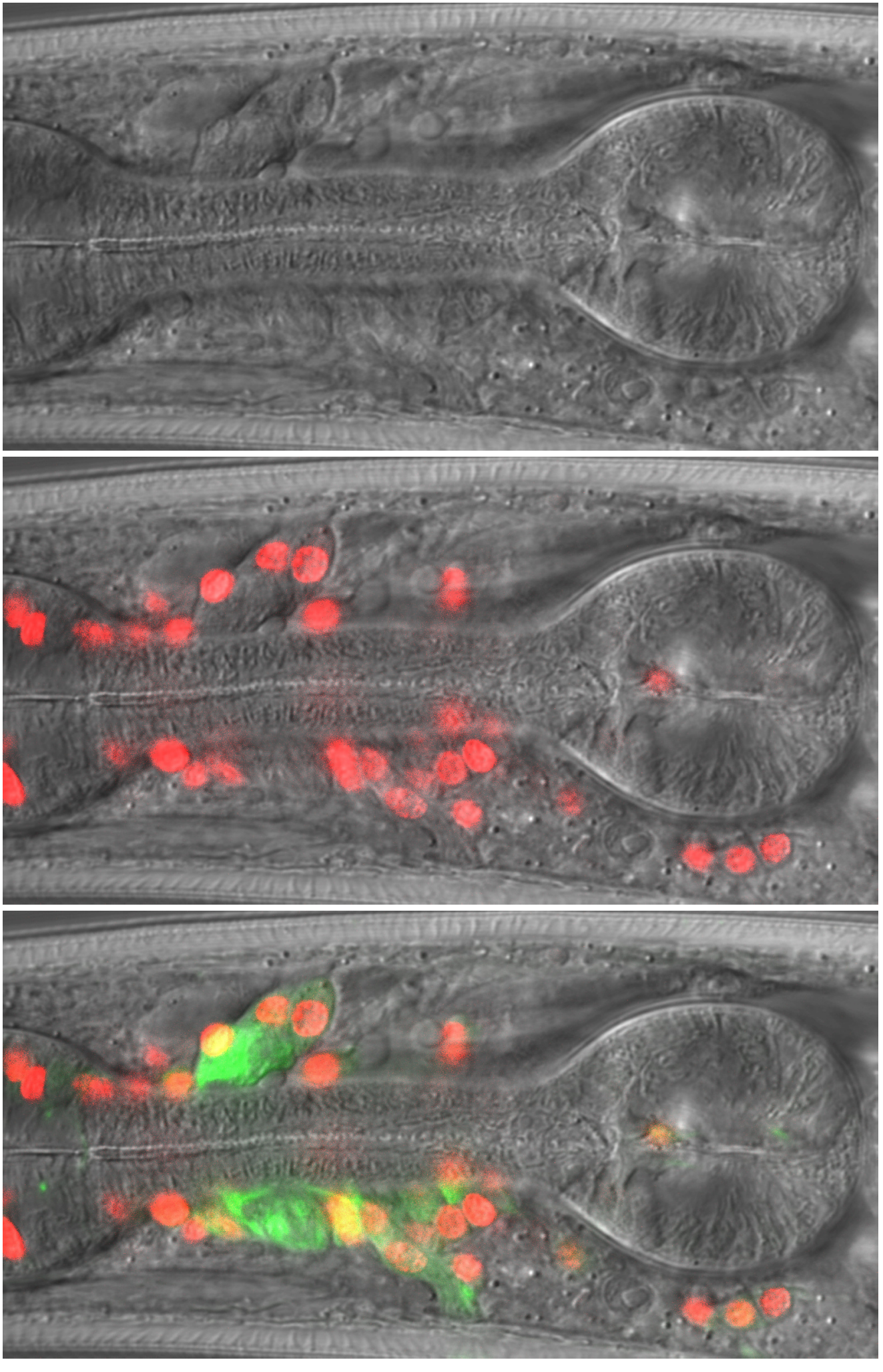

Slice 15

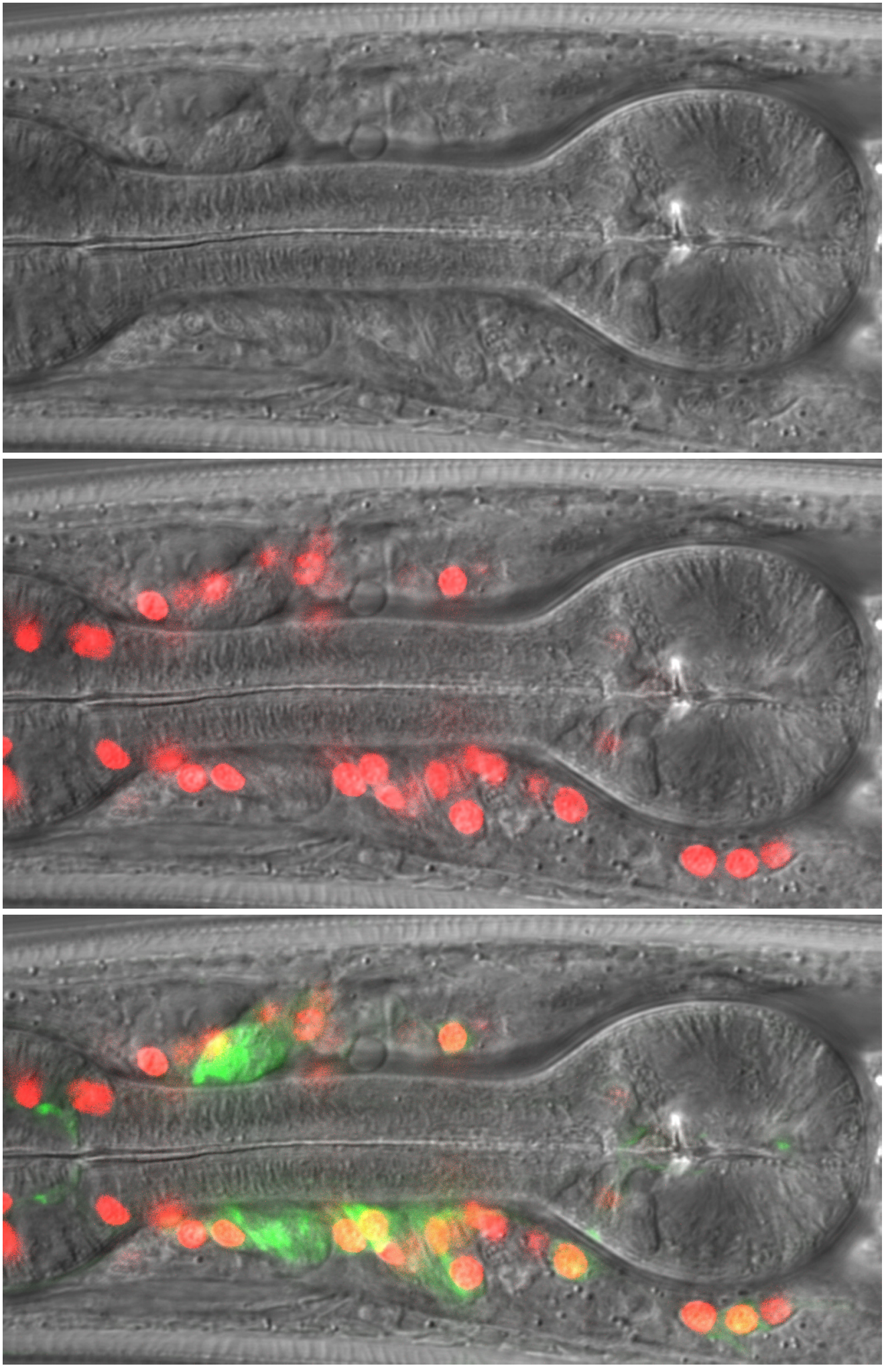

Slice 16

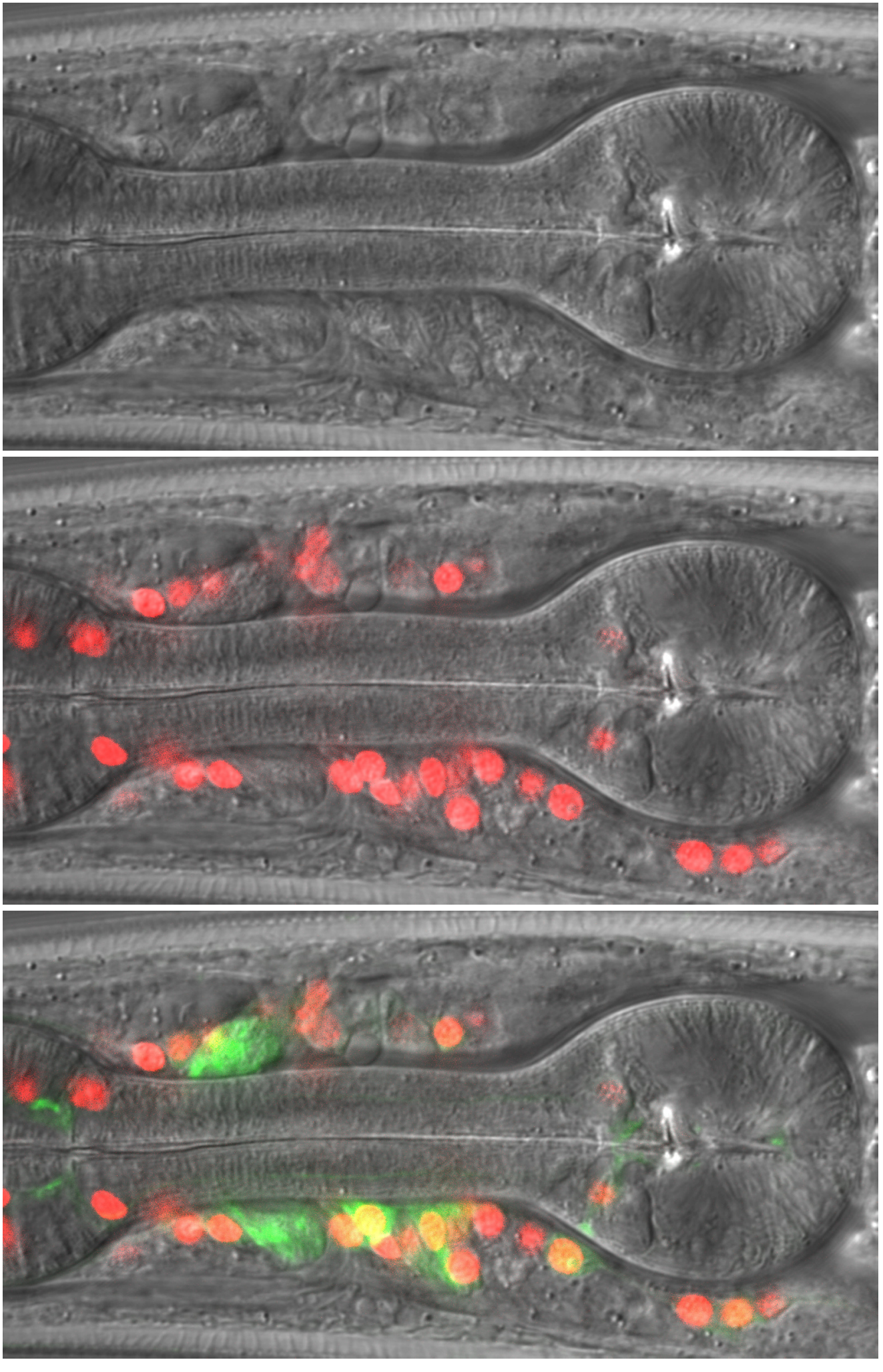

Slice 17

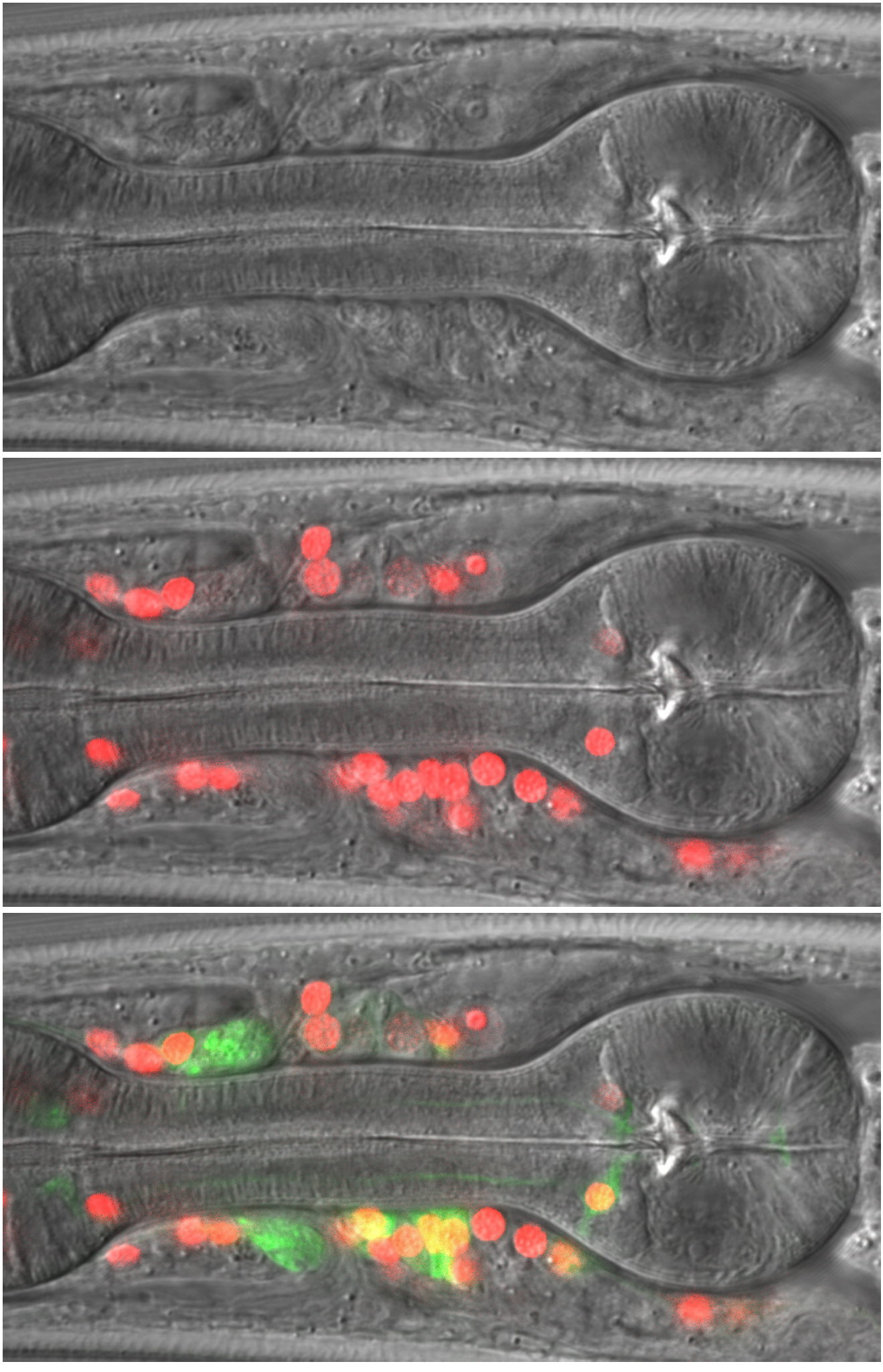

Slice 18

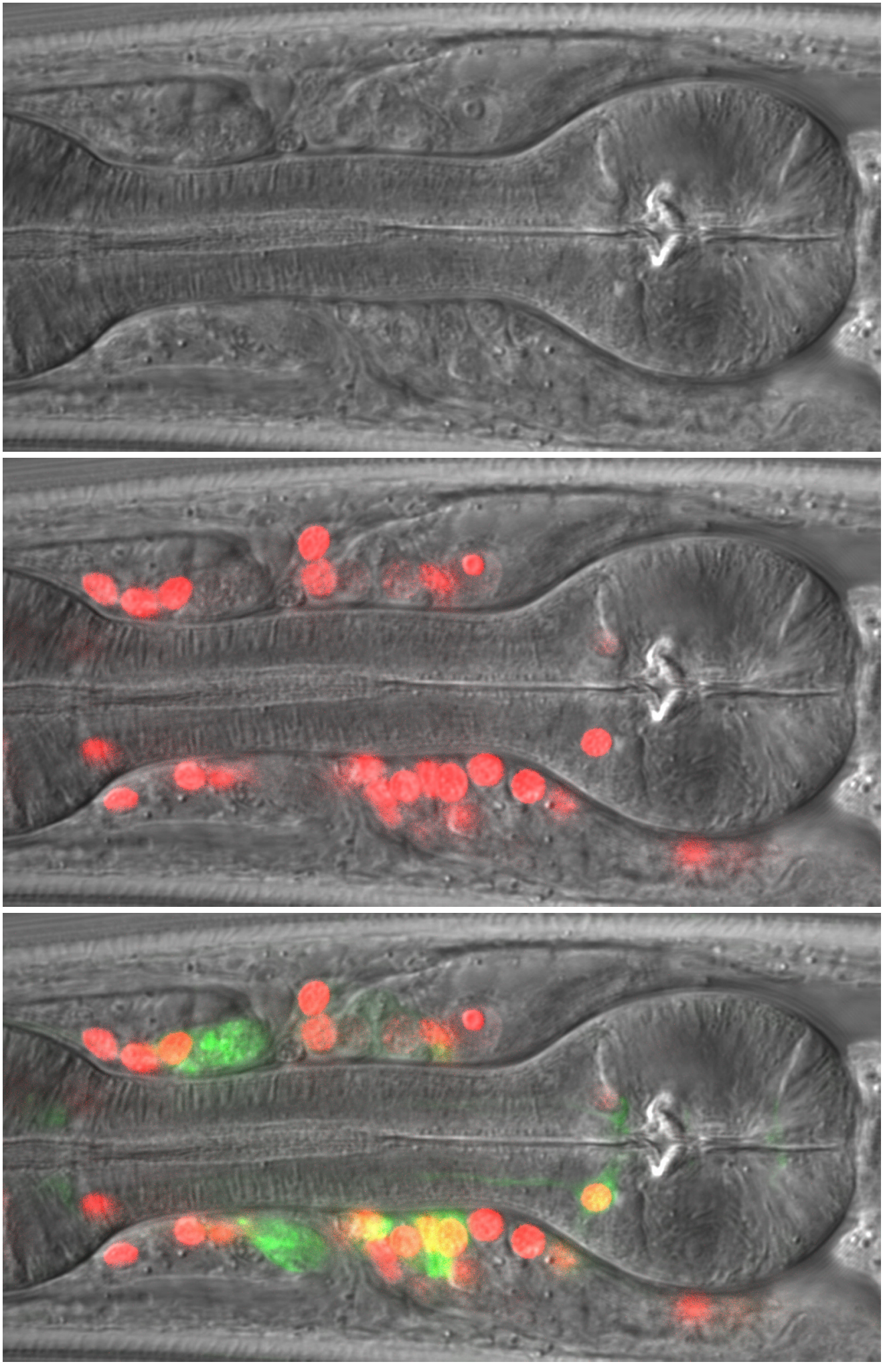

Slice 19

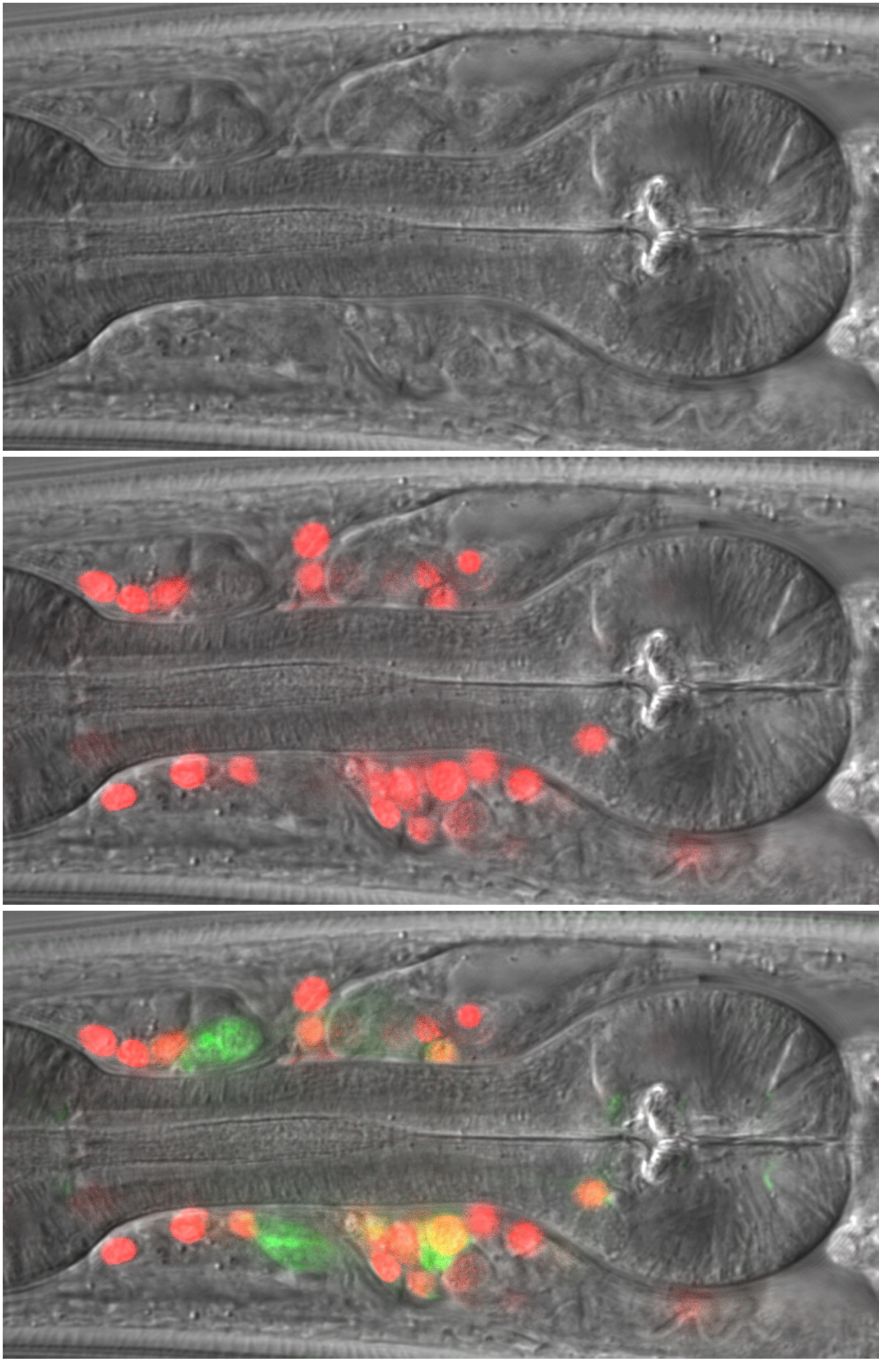

Slice 20

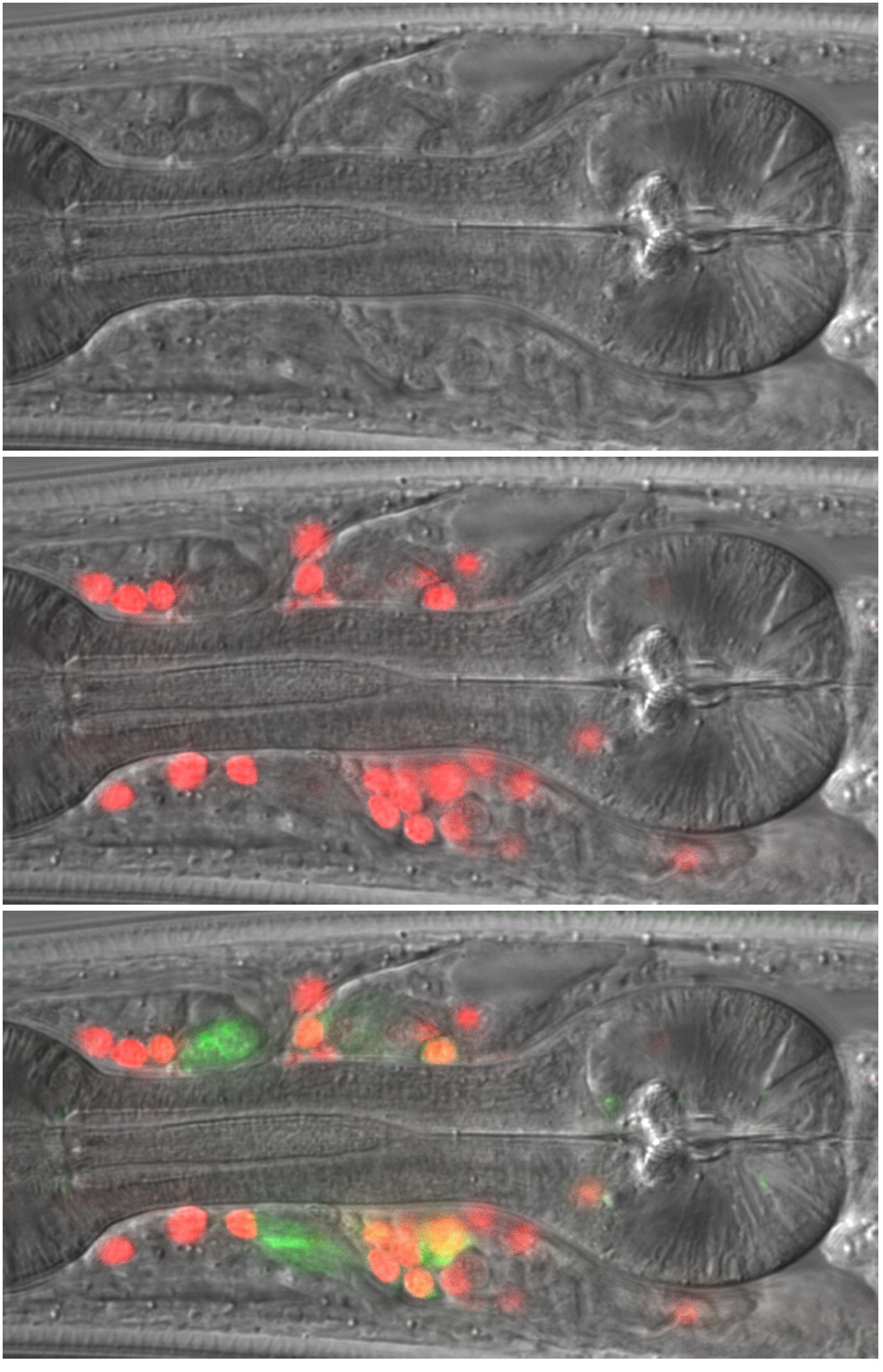

Slice 21

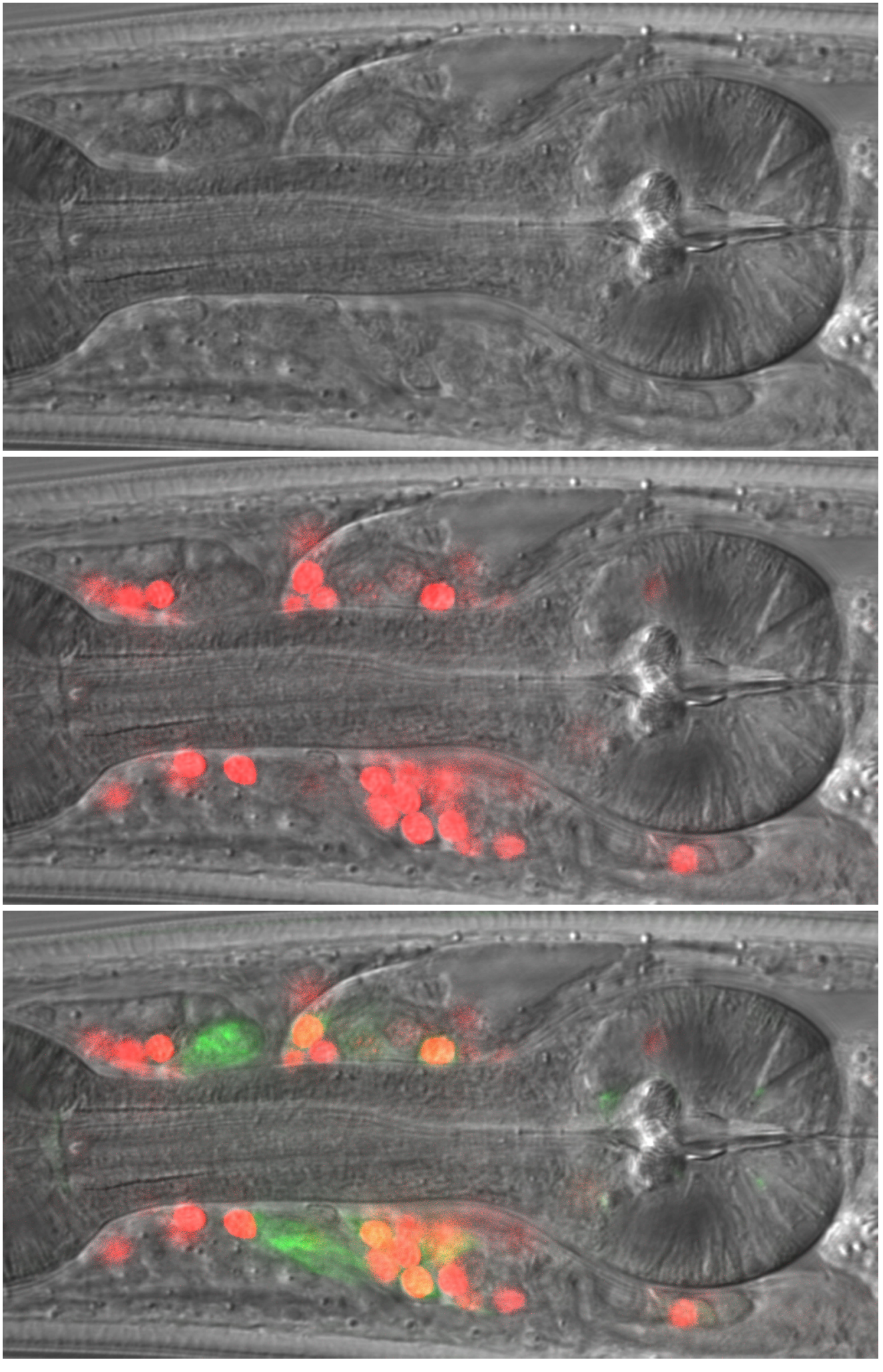

Slice 22

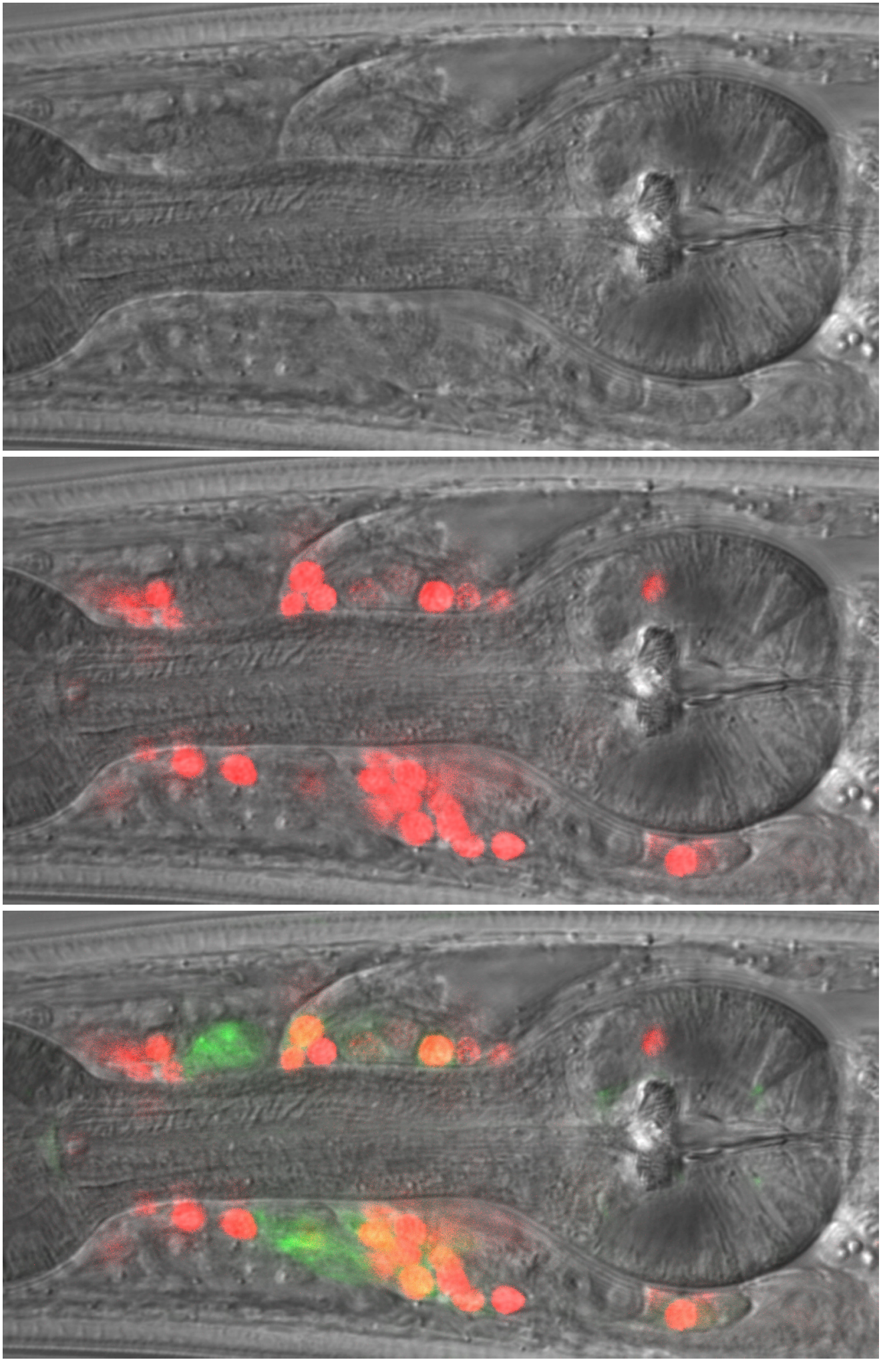

Slice 23

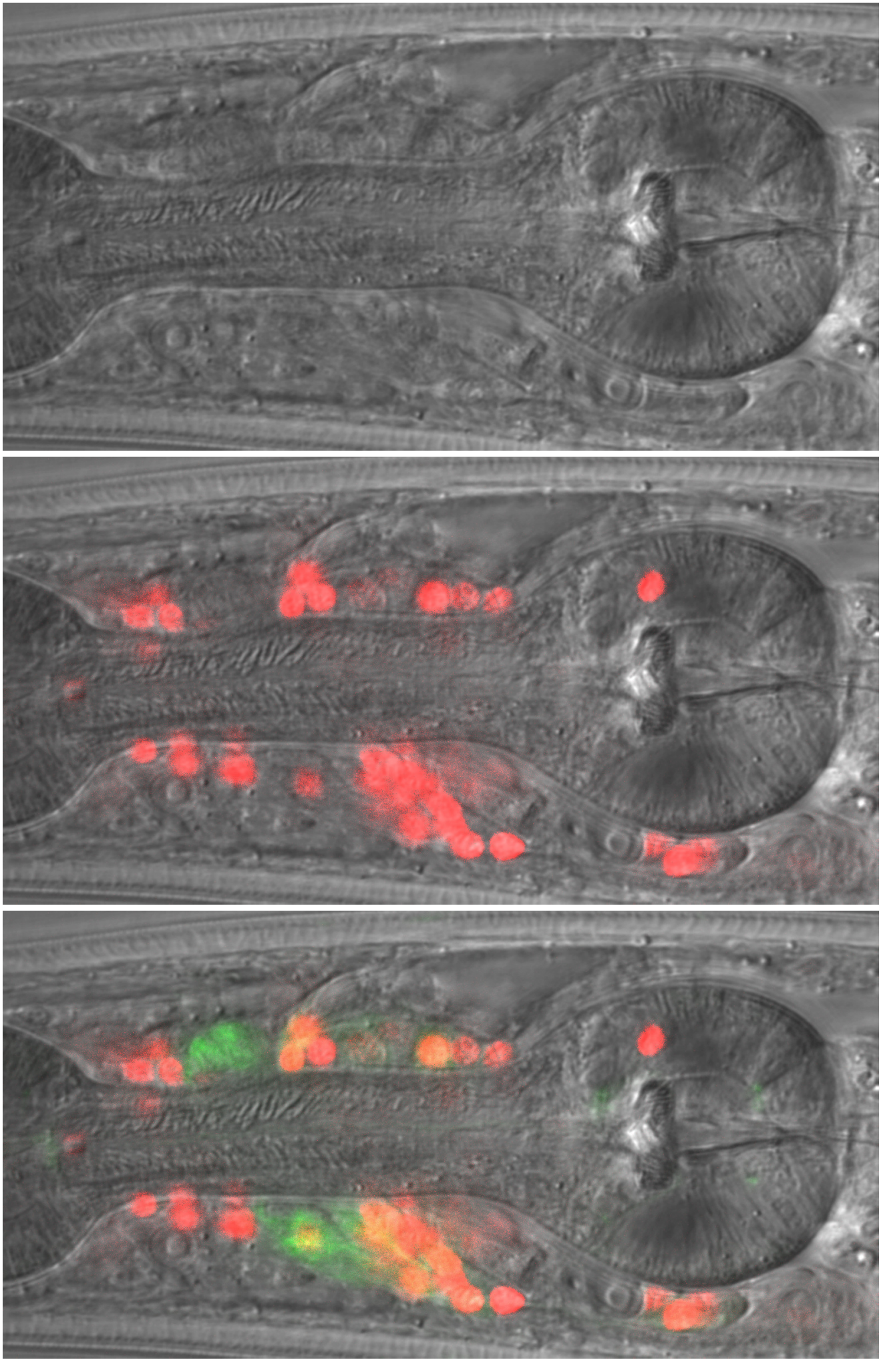

Slice 24

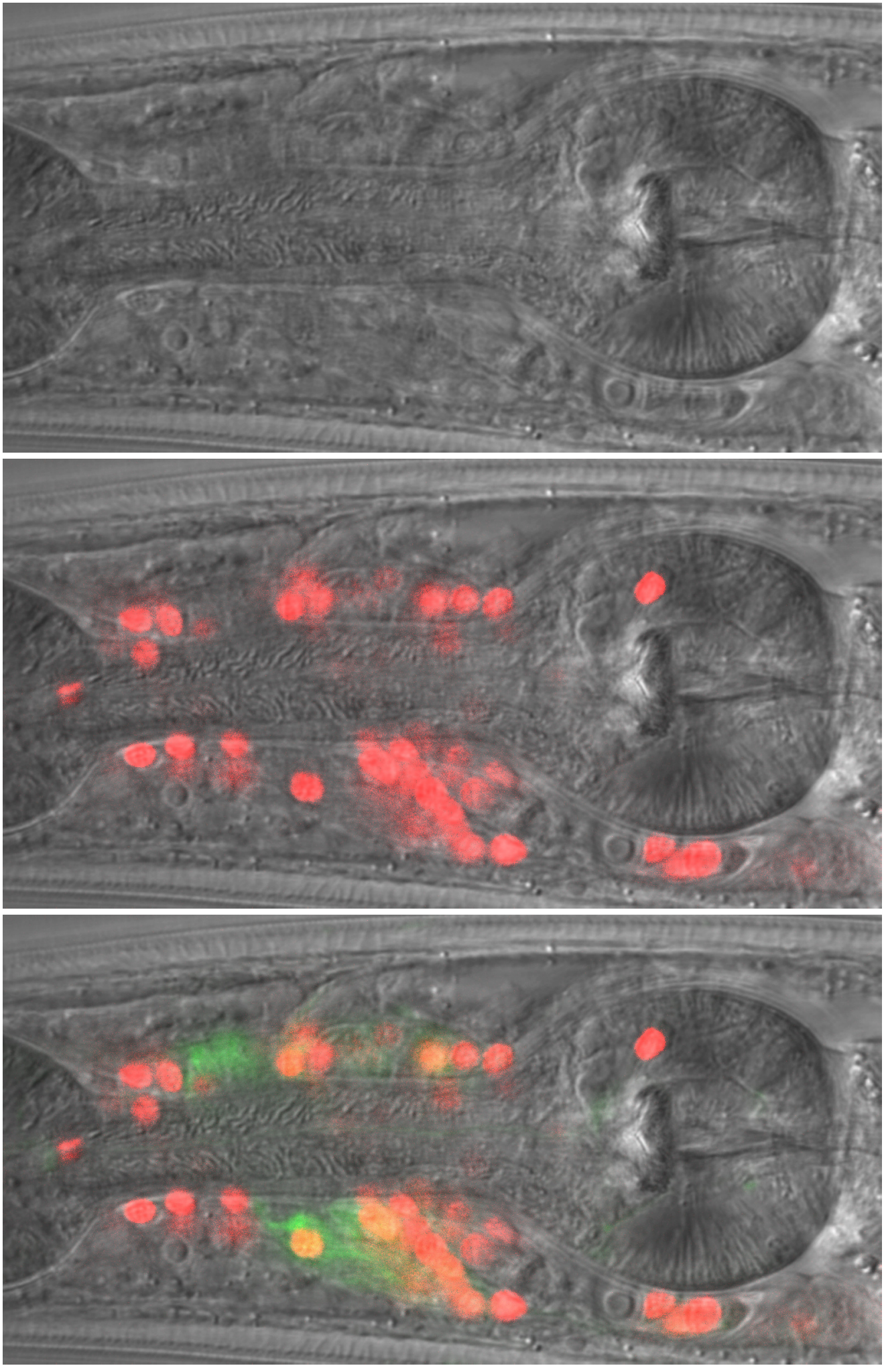

Slice 25

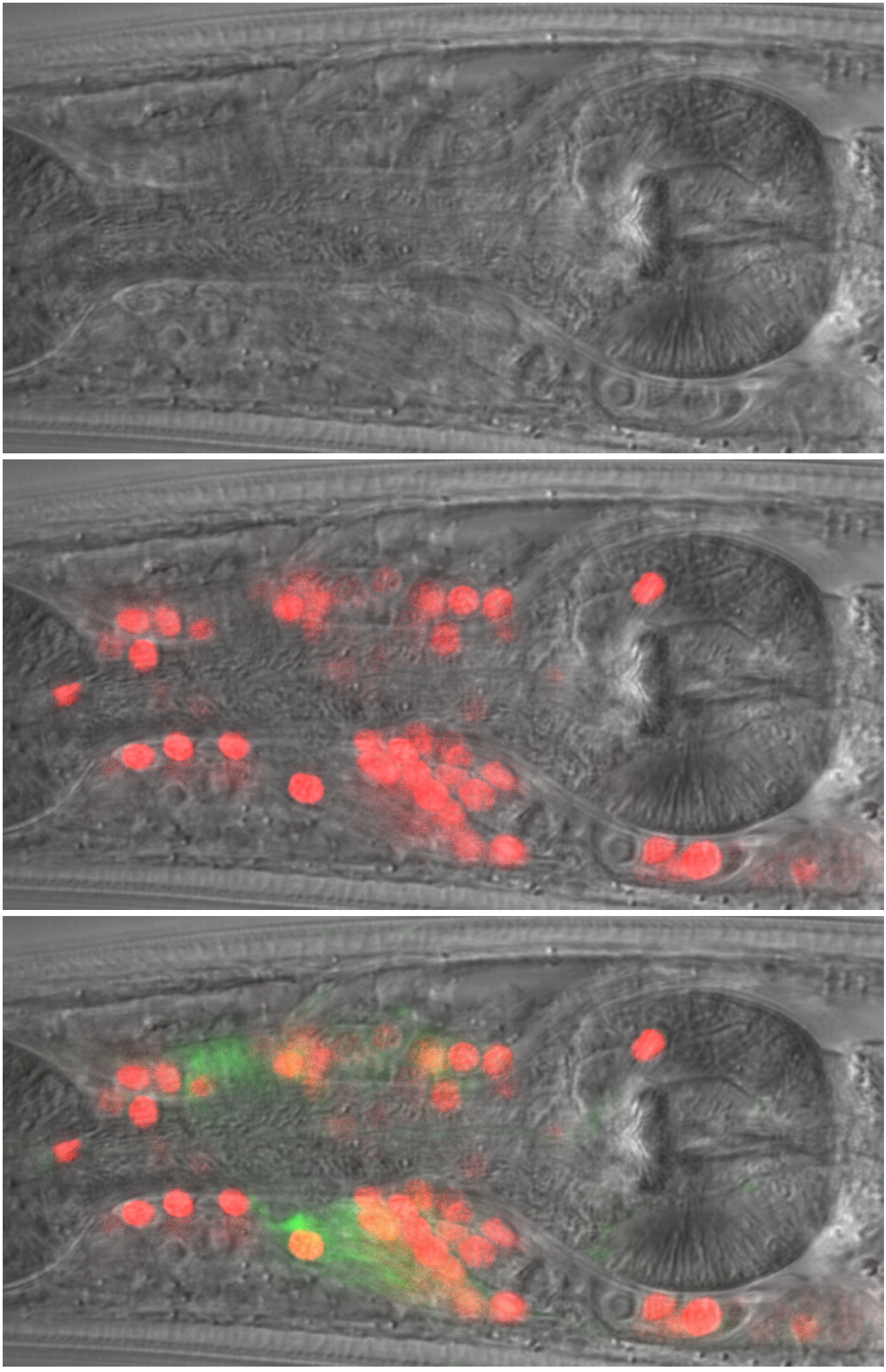

Slice 26

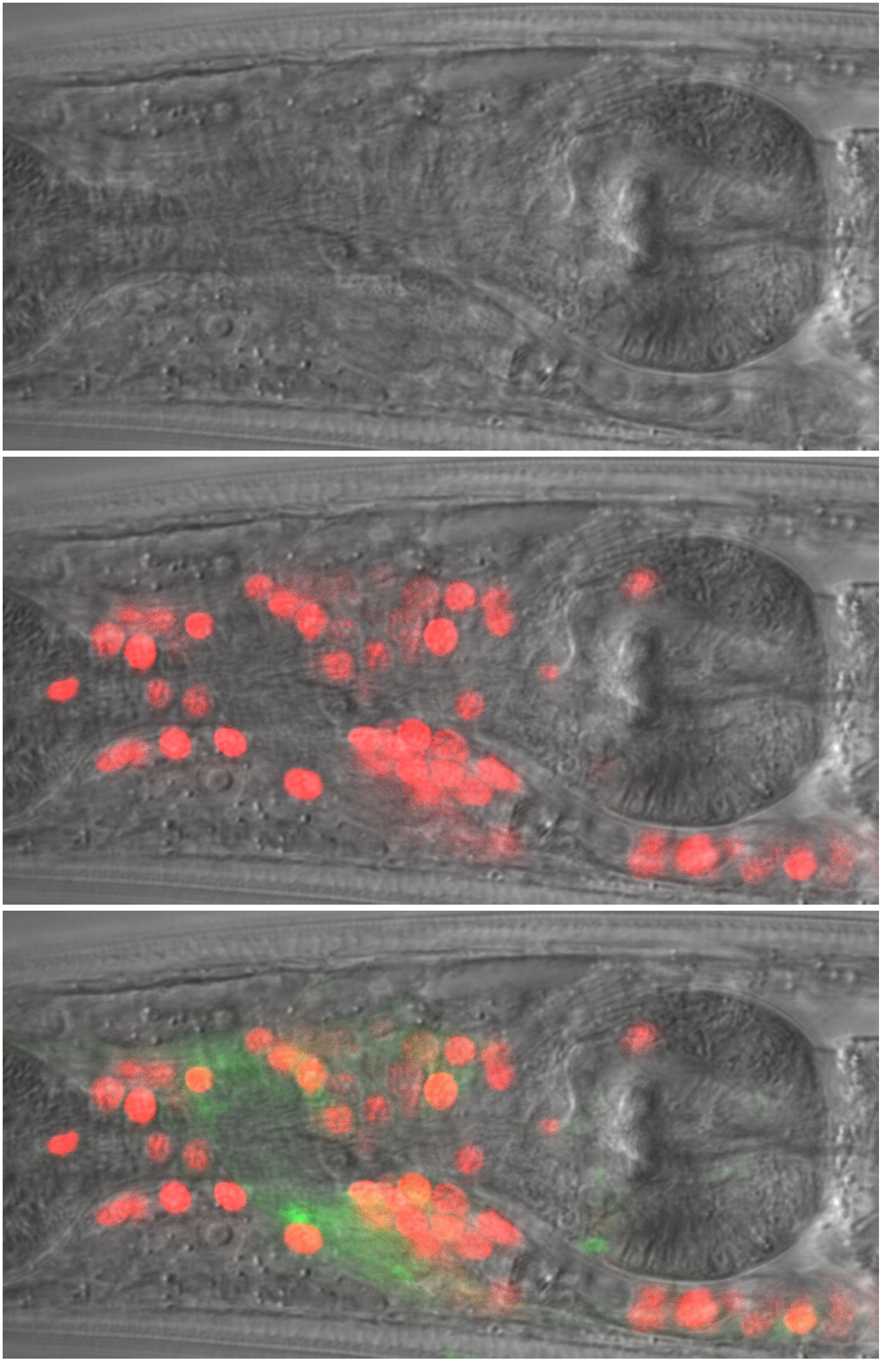

Slice 27

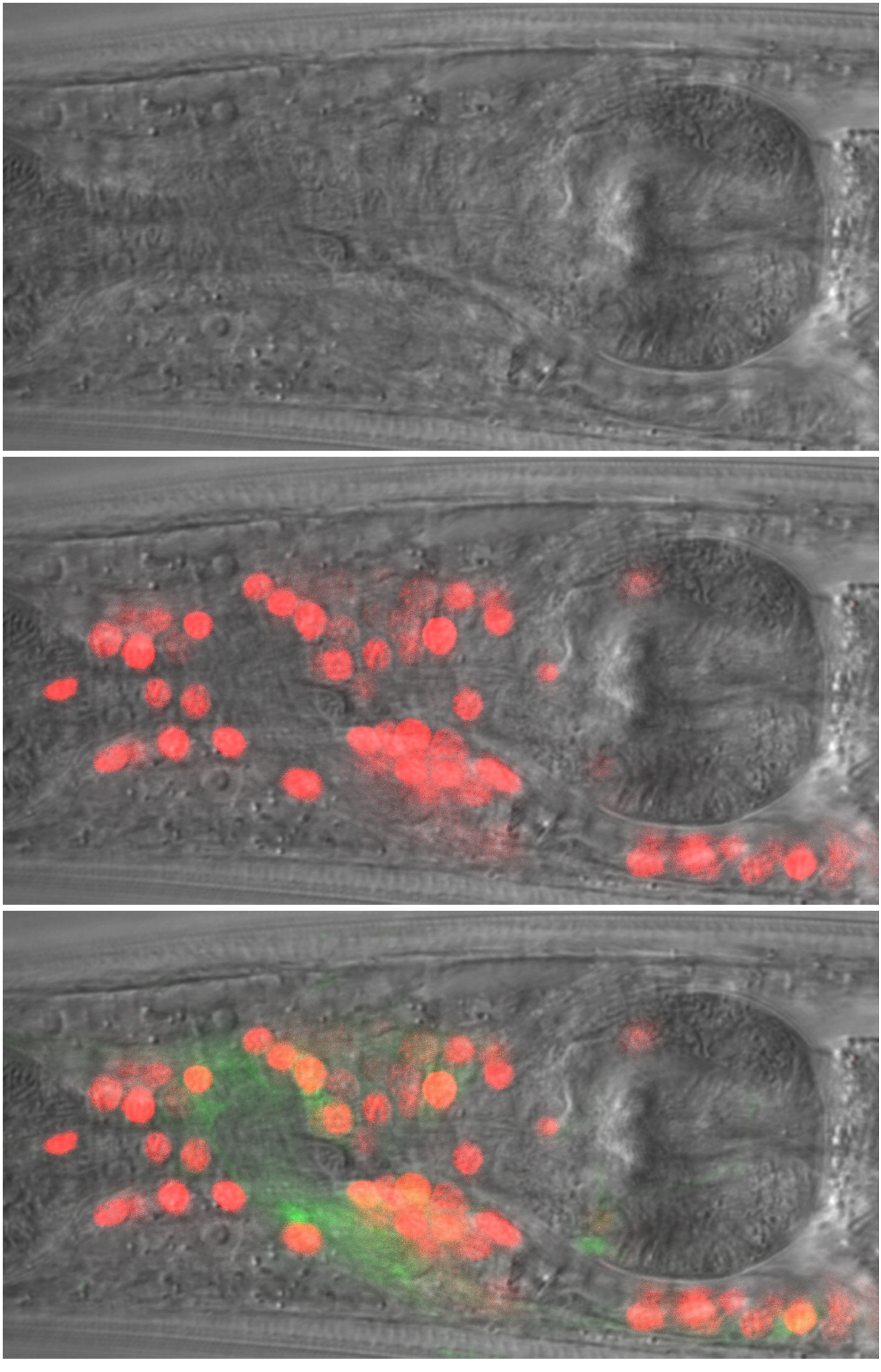

Slice 28

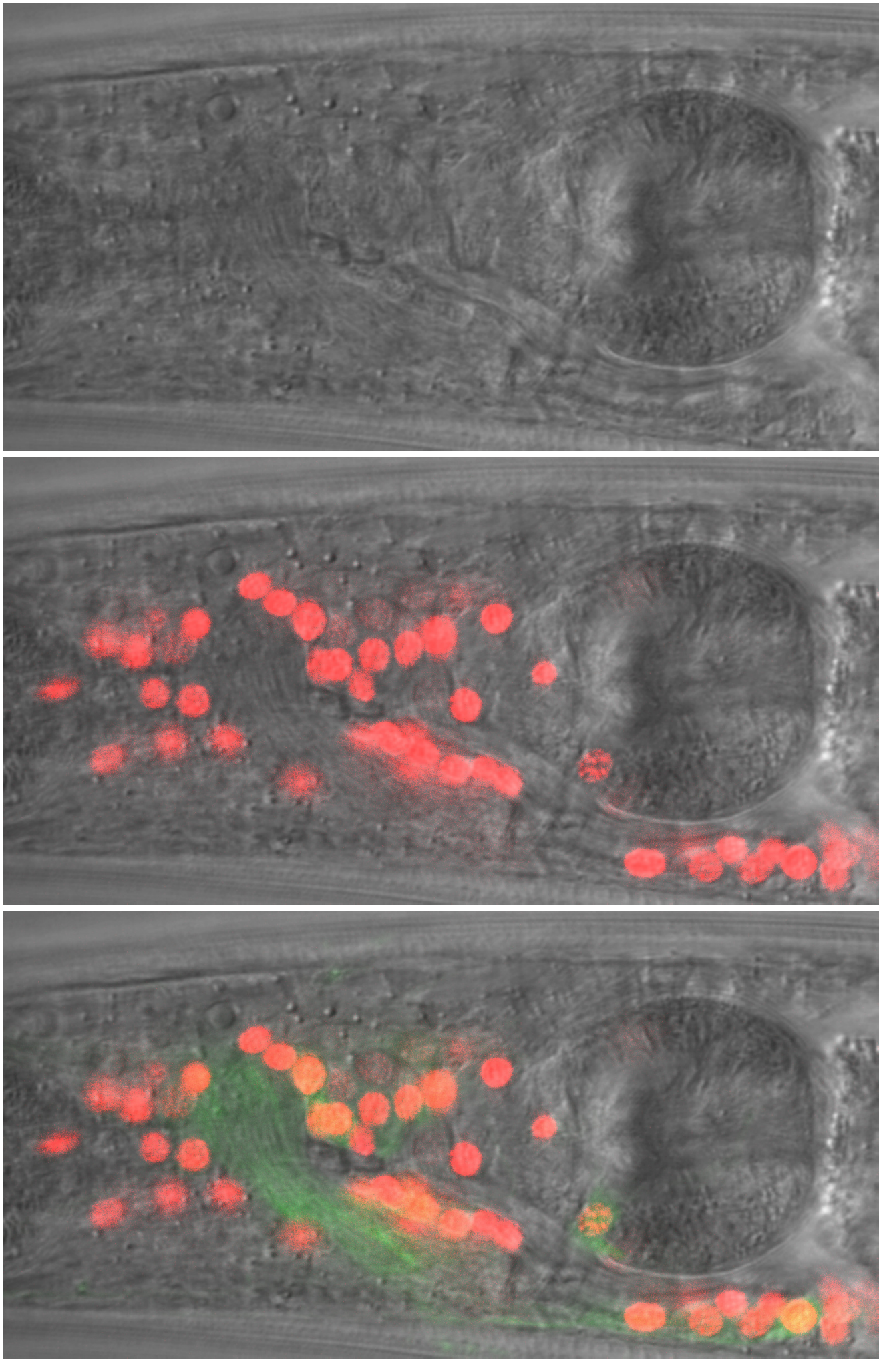

Slice 29

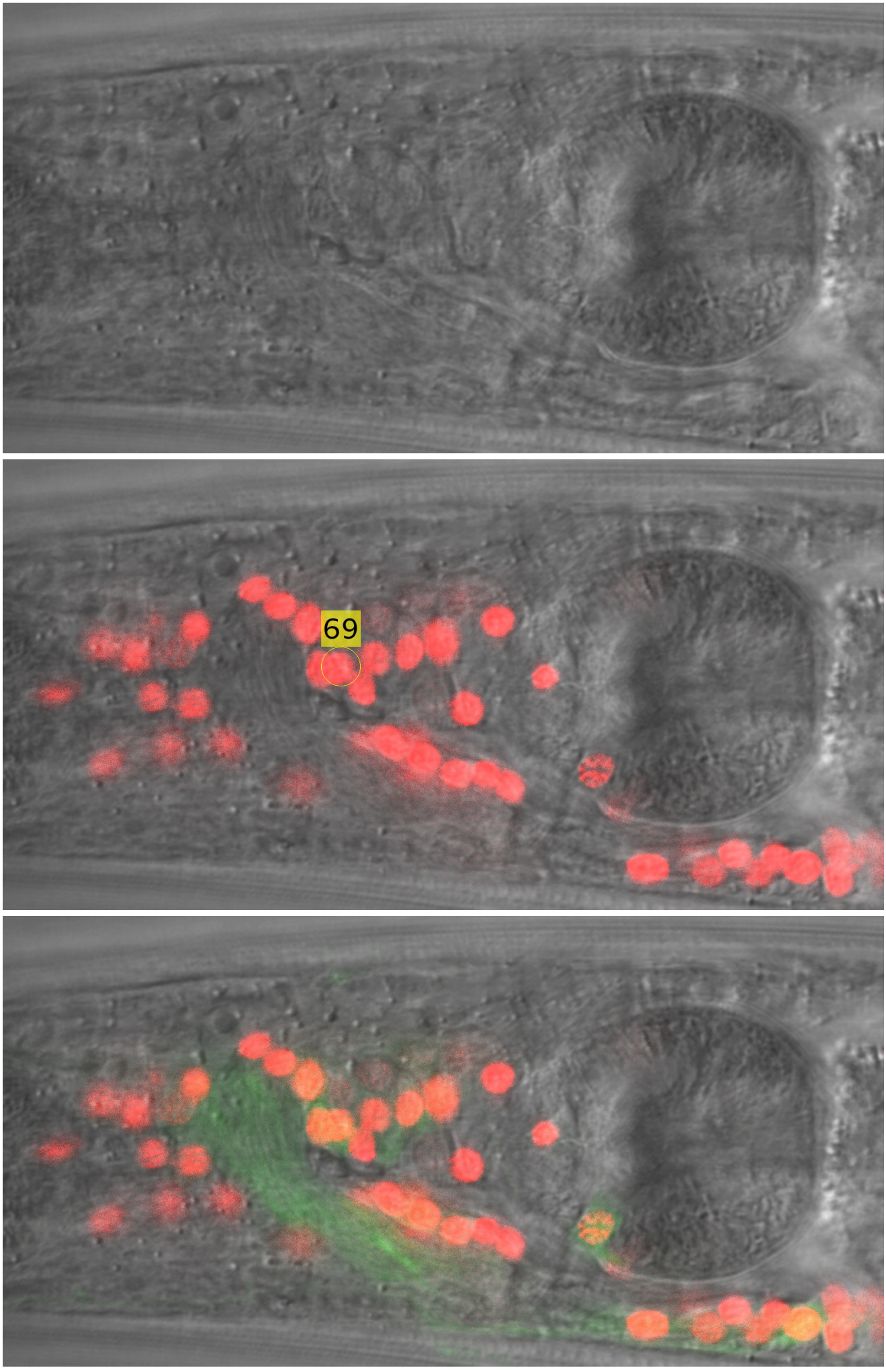

Slice 30

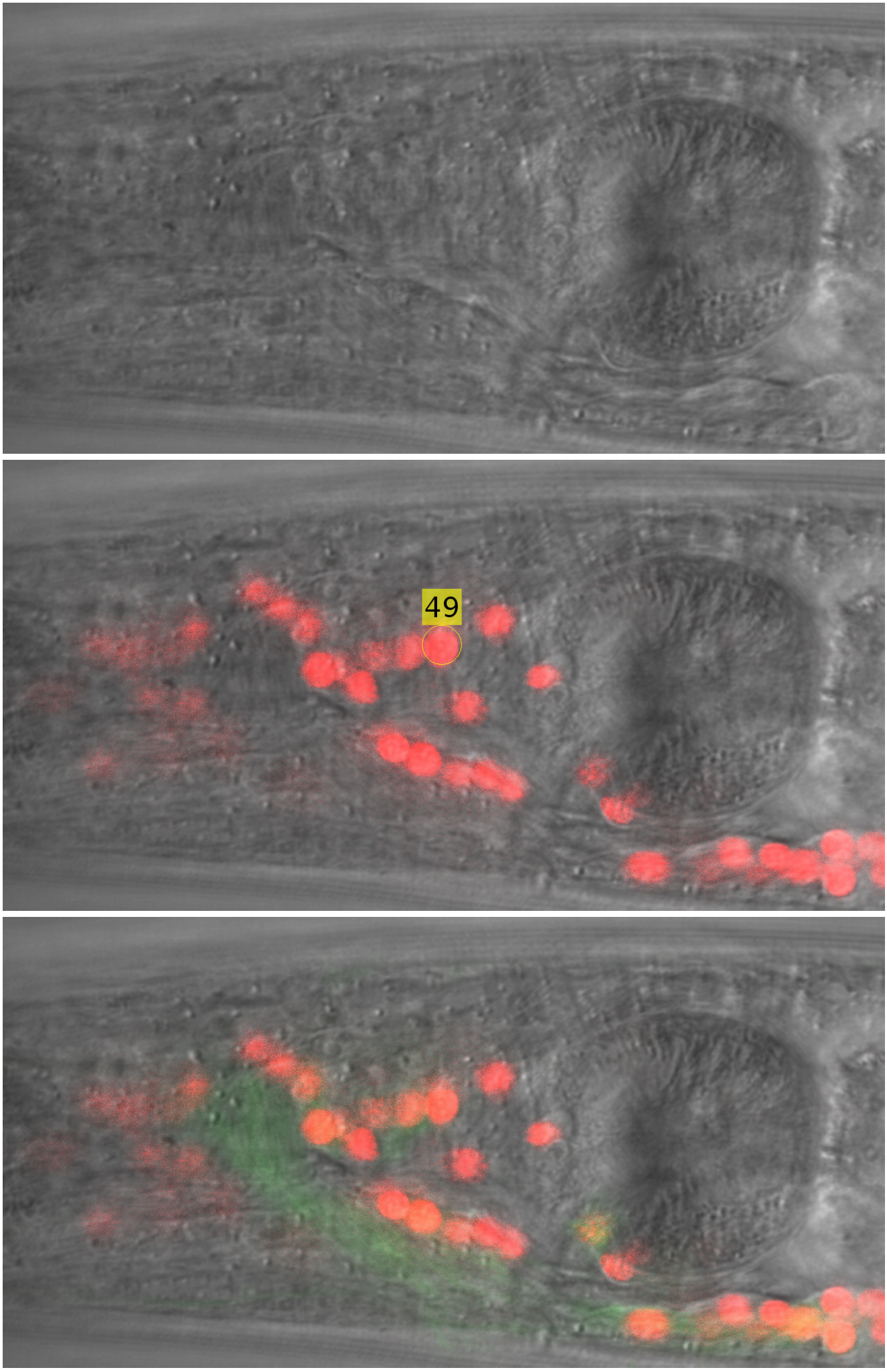

Slice 31

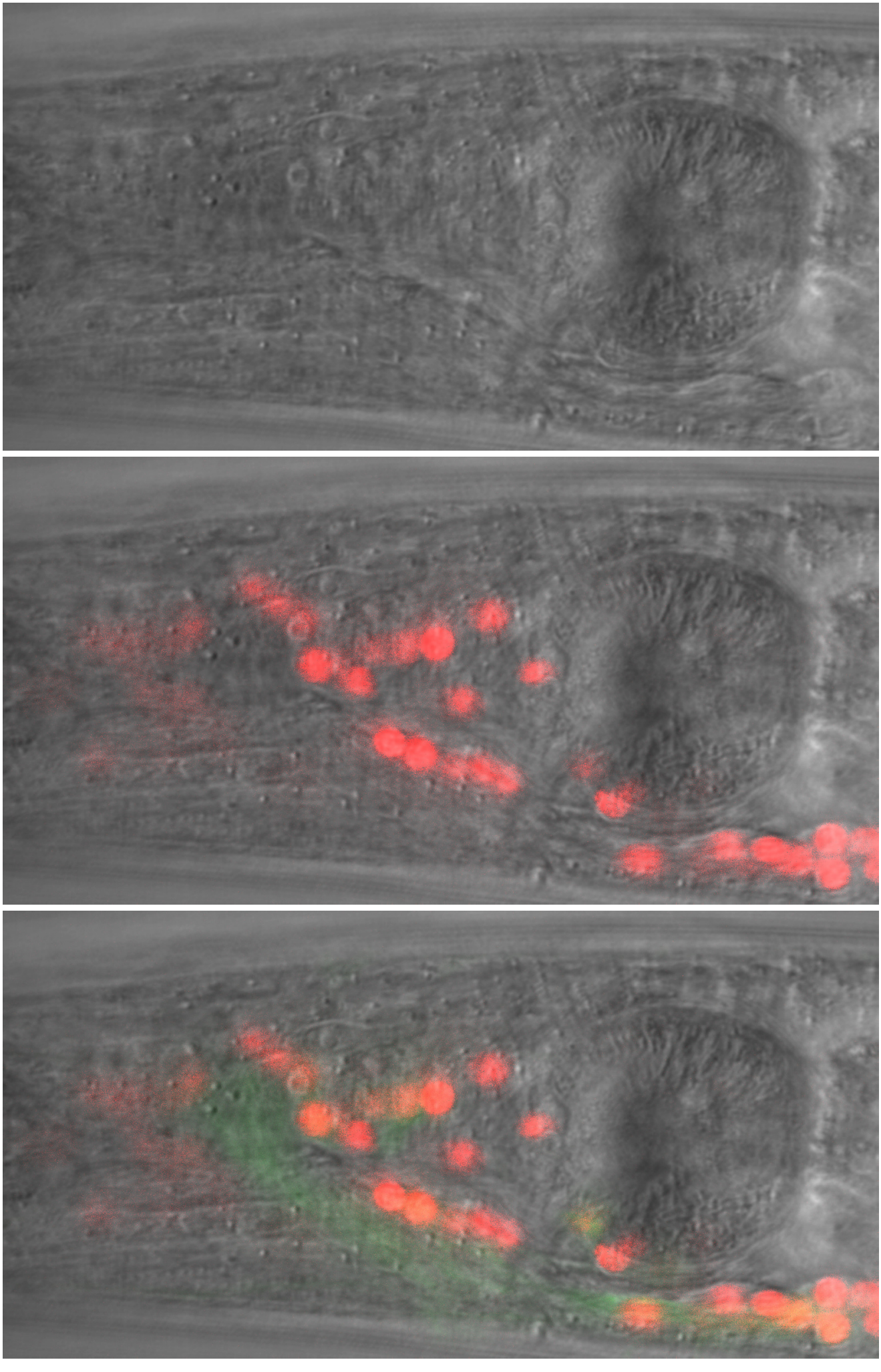

Slice 32

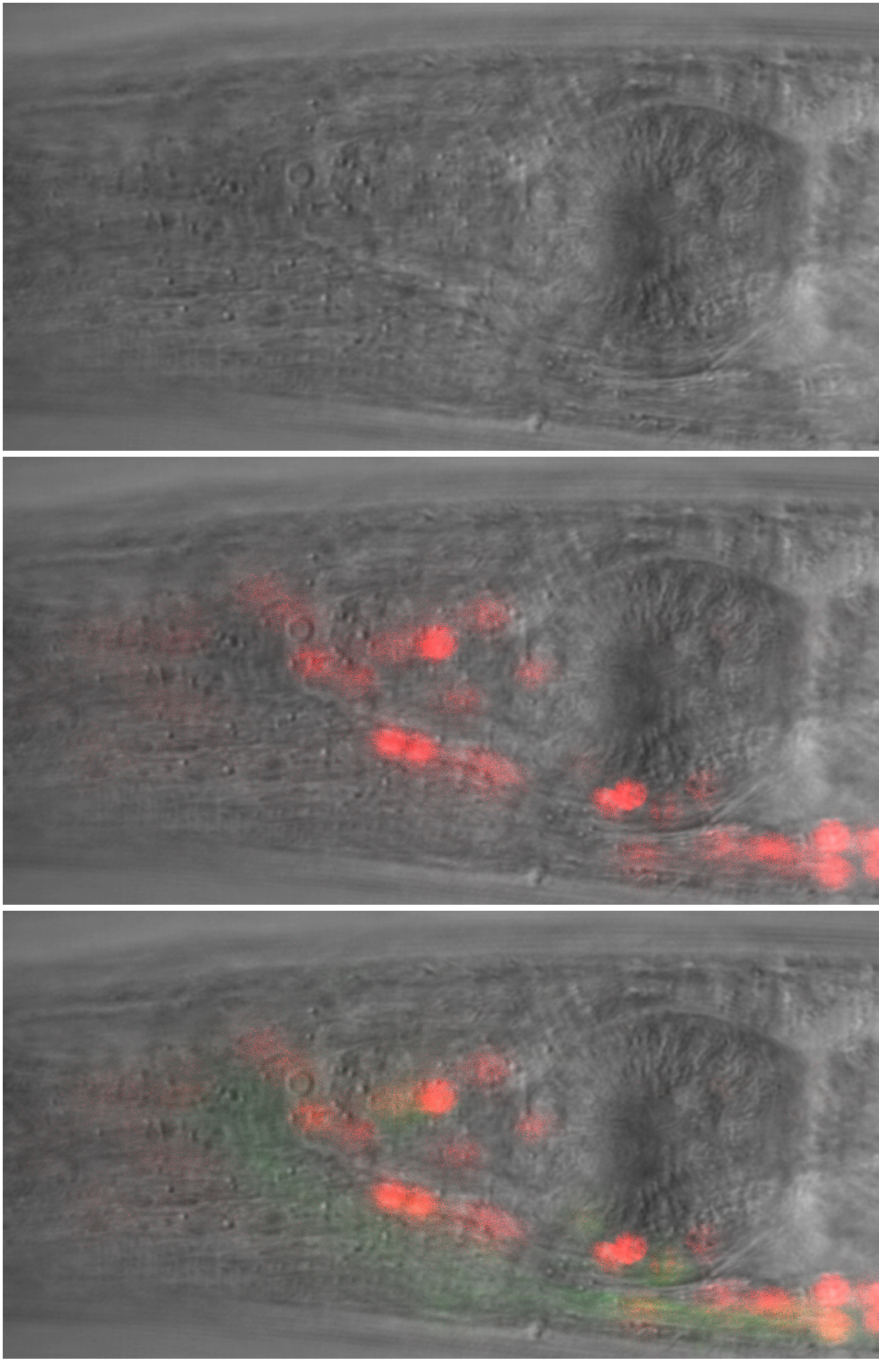

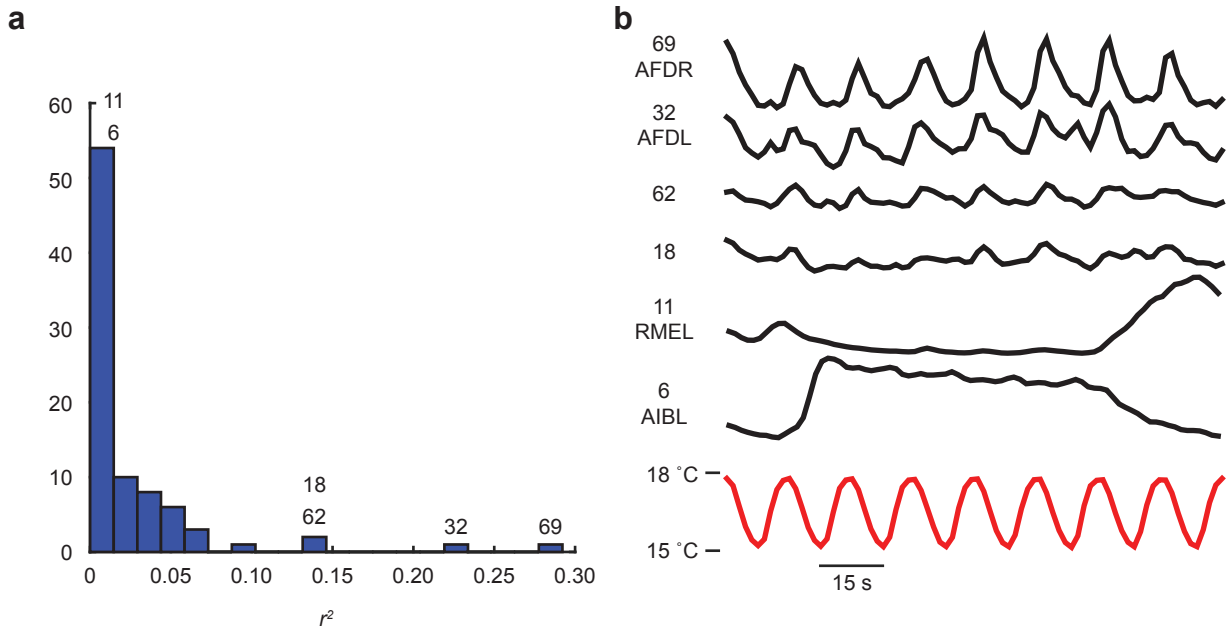
a
60
50
40
30
20
10
0
11
6
18
62
32
69
0
0.05
0.10
0.15
0.20
0.25
0.30
r²
b
69
AFDR
32
AFDL
62
18
11
RMEL
6
AIBL
18 ˚C
15 ˚C
15 s

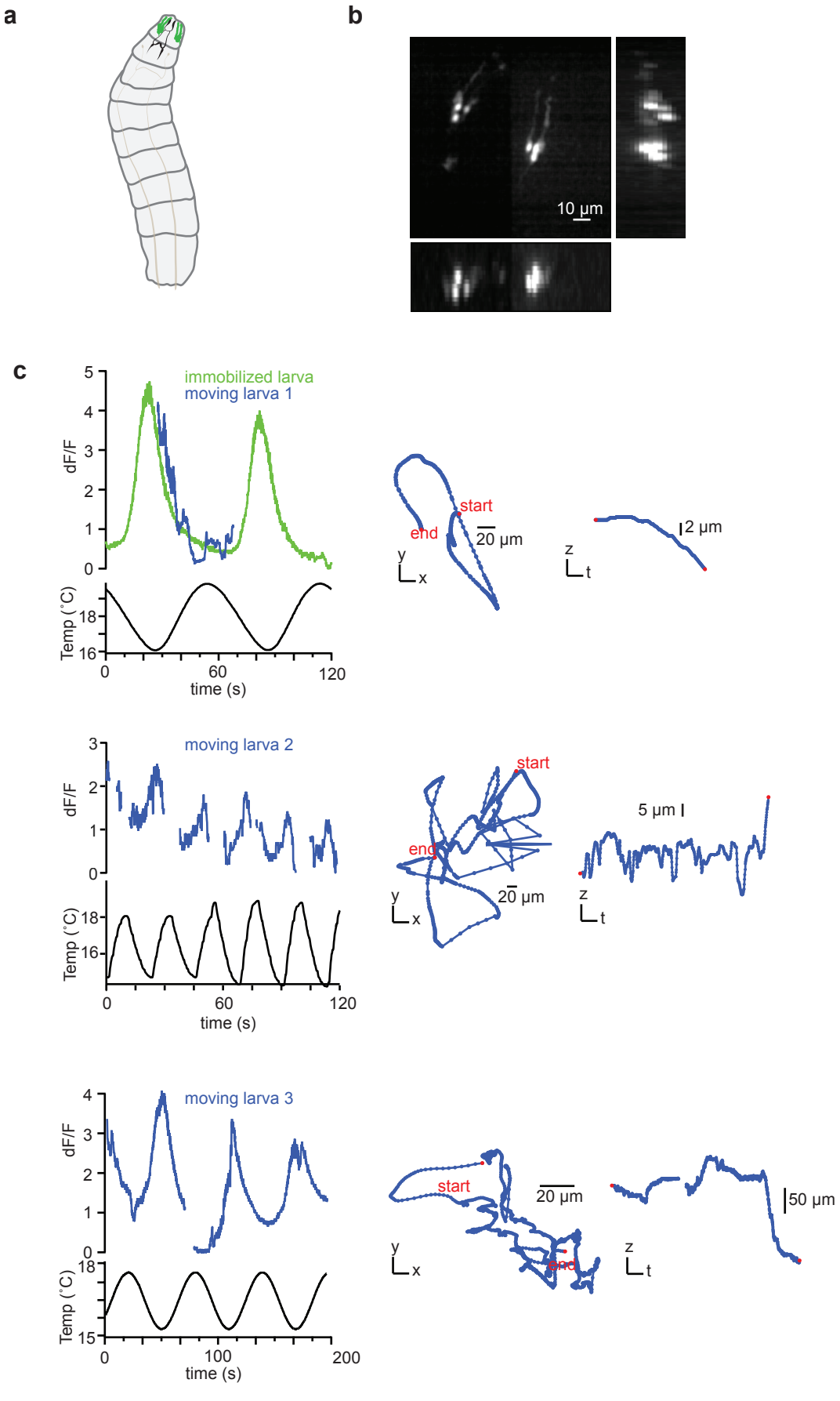
a
b
10 µm
c
immobilized larva
moving larva 1
dF/F
Temp (°C)
time (s)
start
end
20 µm
2 µm
moving larva 2
5 µm
moving larva 3
50 µm

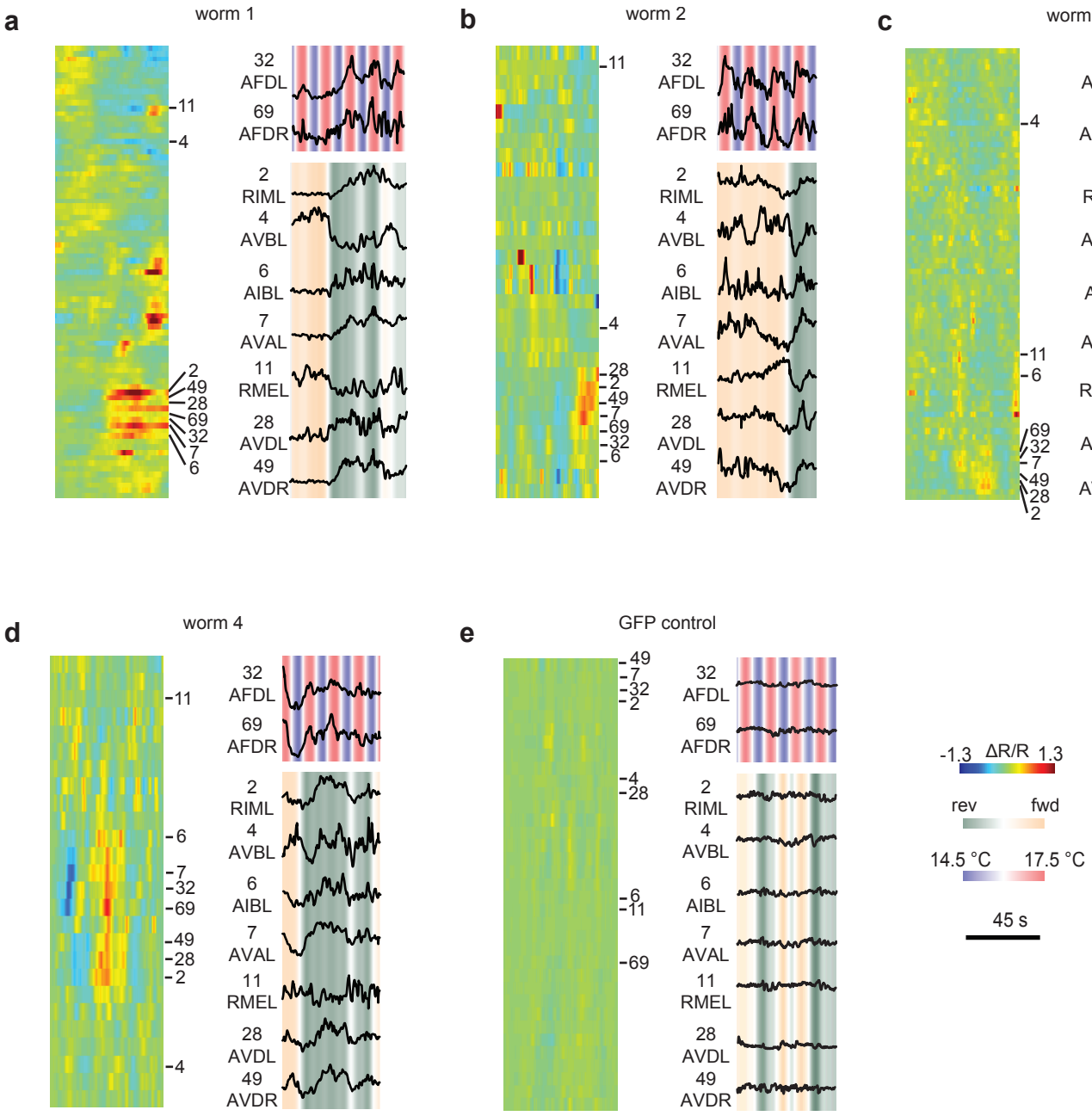
a
worm 1
-11
-4
2
49
28
69
32
7
6
32 AFDL
69 AFDR
2 RIML
4 AVBL
6 AIBL
7 AVAL
11 RMEL
28 AVDL
49 AVDR
b
worm 2
-11
-4
-28
-2
-49
-7
-69
-32
-6
32 AFDL
69 AFDR
2 RIML
4 AVBL
6 AIBL
7 AVAL
11 RMEL
28 AVDL
49 AVDR
c
worm 3
-4
-11
-6
-69
-32
-7
-49
-28
-2
32 AFDL
69 AFDR
2 RIML
4 AVBL
6 AIBL
7 AVAL
11 RMEL
28 AVDL
49 AVDR
d
worm 4
-11
-6
-7
-32
-69
-49
-28
-2
-4
32 AFDL
69 AFDR
2 RIML
4 AVBL
6 AIBL
7 AVAL
11 RMEL
28 AVDL
49 AVDR
e
GFP control
-49
-7
-32
-2
-4
-28
-6
-11
-69
32 AFDL
69 AFDR
2 RIML
4 AVBL
6 AIBL
7 AVAL
11 RMEL
28 AVDL
49 AVDR
-1.3 ΔR/R 1.3
rev fwd
14.5 °C 17.5 °C
45 s